RESEARCH REPORT

Contract no. 93/5.10.2011

EXPLORATORY RESEARCH PROJECTS (IDEI)

Project:

The geomagnetic field under the heliospheric forcing. Determination of the internal structure of the Earth and evaluation of the geophysical hazard produced by solar eruptive phenomena

Stage IV (2014)

Project Director,

Dr. Crişan Demetrescu
Corresponding Member of the Romanian Academy

December, 2014

Content

Introduction

The proposed research aims at achieving an understanding of the space weather effects on conducting structures inside the Earth and on the surface electric field, with applications to a better knowledge of the internal structure of the Earth at continental (Europe) and country scales, on one hand, and to estimating the geophysical hazard of space weather at midlatitudes, on the other. The main objectives are:

1. To derive the magnetic and electrical properties of the terrestrial lithosphere and mantle at continental and Romanian territory scales;

2. To analyze solar eruptive processes and solar wind components responsible for geomagnetic hazardeous activity (geomagnetic storms and substorms) in the time interval 1964-2014;

3. To model the geoelectrical field at the Earth's surface as produced by various magnetospheric and ionospheric current systems;

4 To evaluate the geophysical hazard for technological networks associated to variations of the geoelectric field during geomagnetic disturbances linked to the interaction of solar coronal mass ejections and high speed streams with the magnetosphere.

The initial contract underwent alterations because of budget cuts, so for 2014, according to the additional agreement signed with UEFISCDI, the objectives read:

- Analysis of solar eruptive processesand solar wind, responsible for the hazardeous geomagnetic activity (geomagnetic storms with Dst<-150nT) in the solar cycle no. 23;
- Determining magnetic and electric structure of terrestrial litosphere and mantle at Romanian territory and European continental scales;
- Modelling the surface geoelectric field;
- Preparing the research report and dissemination of results.

The research report for the stage 2014 is structured in chapters, according to the work plan, as follows:

In *Chapter I,* entitled "**Analysis of solar eruptive phenomena and solar wind, responsible for hazardeous geomagnetic activity (storms with Dst < -150 nT) in solar cycle 23. Geomagnetic efficiency modelling of eruptive phenomena**", the results of two

studies, one concerning the geo-effectivity of the coronal mass ejections (CMEs) and of interplanetary mass ejections (ICMEs), and the other concerning the geo-effectivity of the high speed streams (HSSs), with a special emphasis on the solar cycle 23, are presented.

In *Chapter II*, entitled "**New geomagnetic and magneto-telluric measurements in Romania**" the geomagnetic measurements carried out in 2014 at the 26 repeat stations of the National secular variation network and at the Surlari geomagnetic observatory, as well as the results of two magneto-telluric determinations carried out in the Transylvanian Depression, are described.

In *Chapter III*, entitled "**Determination magnetic and electric structure of terrestrial litosphere and mantle at Romanian and continental scales. A 3D model of the electrical resistivity distribution on the Romanian territory**", two models of the distribution of electric properties of lithosphere and mantle are presented, one for the European continent, using data from the geomagnetic observatory network and data for a number of geomagnetic storms, and a second one, for the Romanian territory, using magneto-telluric measurements. In the first case the magnetic/electromagnetic induction model, previously devised by research team members. In the second case the electric structure of the crust on the Romanian territory is presented, as a block model with vertical variation of the electrical resistivity in each block.

In *Chapter IV*, **e**ntitled **"Toward a model for the surface geoelectric field produced by hazardeous geomagnetic variations. Case study – the Romanian territory",** preliminary results on the possible magnitude of the surface geoelectric field that generates geophysically induced currents in Romania, based on the only geomagnetic observatory records in Romania, at the Surlari observatory, are presented.

In *Chapter V*, entitled "**Dissemination of results**", the list of published papers and of presentations at scientific meetings in 2014 is presented. We mention that the web page of the project was updated. The address is: http://www.geodin.ro/IDEI2011/engl/index.html.

Chapter I: Analysis of solar eruptive phenomena and solar wind, responsible for hazardeous geomagnetic activity (storms with Dst < -150 nT) in solar cycle 23. Geomagnetic efficiency modelling of eruptive phenomena

1.1. The contribution of solar eruptive phenomena to major geomagnetic storms in solar cycle 23

1.1.1. Introduction

The influence of eruptive solar processes over the Earth is a subject of great importance in present times in the context generated by satellite space missions that study both the Sun and the heliosphere. The first observation of an eruptive phenomenon – a strong flare in white light – with geomagnetic consequences was that one made independently by Carrington (1859) and Hogson (1859). Since then Sun observations have undergone an immense progress, such that today we benefit of full disk images in many wavelengths, images of the magnetic configuration of the Sun, as well as many other measurements, close to Earth, that allow to evaluate the terrestrial magnetic field, the conditions of the interplanetary magnetic field, and information about the particle flux that reaches the Earth. All these help us to analyse in detail the influence of solar wind together with the solar eruptive phenomena.

This study is based on the data provided by the SOHO mission (Solar and Heliospheric Observatory), mission that is composed of 12 instruments amongst which LASCO (Large Angle and Spectrometric Coronograph) (Brueckner et al. 1995) that provides white light images of the solar corona, on the coronal mass ejection catalogue maintained by CDAW Data Center from NASA and by The Catholic University of America in cooperation with the Naval Research Laboratory, as well as on the data from IMP 8, Geotail, Wind and ACE, available through the interface OMNIWEB (http://omniweb.gsfc.nasa.gov) maintained by Goddard Space Flight Center – NASA.

Interplanetary coronal mass ejections (ICME) are those coronal mass ejections (CME) that are observed in the interplanetary space. Generally, ICMEs are detected through a series of characteristic signatures: the sudden increase in speed, the increase of the magnetic field, the rotation of the magnetic field, the decrease of the density and temperature of electrons etc. (Zurbuchen and Richardson, 2006). Few of these events have all the signatures, usually only three signatures are necessary to identify an interplanetary coronal mass ejection, namely the total pressure perpendicular on the

magnetic field in the interplanetary medium close to 1AU, the maximum value of the intensity of the interplanetary magnetic field, B_{max}, and the speed variation, i.e. the difference between the maximum and minimum speed (ΔV) of the solar wind during that specific event (Jian et al. 2006). Generally, an ICME is defined as the entire perturbation, comprising the shock (if it exists), the shield, the region of solar wind compression, "the driver" or ejecta, and the back of the ejecta or the feet of the coronal mass ejection (Rouillard, 2011).

1.1.2. Event Selection

Solar cycle 23 (during 1996-2008) had a number of 29 intense storms with a Dst minimum value less than -150 nT. Using the Richardson and Cane catalogue (available and updated online) we have identified the interplanetary coronal mass ejections corresponding to those geomagnetic storms, and we noticed that all geomagnetic intense storms were triggered by interplanetary coronal mass ejections.

In order to identify the coronal mass ejections responsible for triggering interplanetary CMEs we used the Richardson & Cane catalogue to which we have added data obtained by Zhang et al. (2007). Appendix 1 shows a summary table containing all storms characterised by a minimum Dst value lower than -150 nT and of their connection to solar eruptive phenomena. Columns show the perturbation date, the beginning and end of the interplanetary coronal mass ejections, the increase in speed estimated from the hourly mean values of the solar wind, the ICME speed, the maximum speed recorded in the solar wind, the mean magnetic field intensity inside the ICME, the association with magnetic clouds, the minimum value of the Dst index, the mean transit speed at 1 AU and the solar ejection associated with the corresponding event. Coronal mass ejections that have been introduced from Zhang et al. (2007) have been marked by "*".

From the Richardson and Cane catalogue just two interplanetary coronal mass ejections are not correlated to coronal mass ejections, that is, the event of October 2, 2001 and the one of September 30, 2002, but Zhang et al. (2007) found their corresponding CMEs (See Appendix 1.1, events numbers 14 and 20). The properties specific to these geoeffective CMEs are shown in Table 1.

Out of the 42 coronal mass ejections, only three do not have a linear speed calculated because of LASCO/SOHO data gaps.

There are 9 coronal mass ejections whose interplanetary speed increases as magnitude from the distance of 20 solar radii to the distance of 1 AU. All ejections

change their speed during their propagation towards the Earth, the majority being decelerated because of their interaction with the solar wind, other ejections or solar high speed streams.

Coronal mass ejections of Table 1 are, in their vast majority, of Halo type (angular width larger than 120^0) as seen in the white light images from LASCO/SOHO.

Only 18 CMEs have positive values for the acceleration, which means that most of them are decelerated after the ejection moment in the Sun vicinity. For the exact computation of the accelerations, but especially of their variation in time and as a function of height, one needs data from the lower corona in order to exactly determine its evolution. Studies carried on by St.Cyr et al. (1999) and Zhang et al. (2001) show that the acceleration is greater in the lower corona, that there is no deceleration under three solar radii, despite of gravity. 30% out the coronal mass ejections observed by LASCO/SOHO are decelerated, a percentage that increases to 54% in our selection.

Table 1: General properties of geo-effective coronal mass ejections

Nr. Crt.	CME	Position	V_{liniar} (km/s)	$V_{2nd\ order}$ at final height (km/s)	$V_{2nd\ order}$ at 20 Rs (km/s)	Acce-leration (m/s^2)	$V_{tranzit}$ 1 AU (km/s)
1.	1998/05/02 – 14:06:12 H	S17W24	938	697	871	-28.8	1150
2.	1998/05/02 – 05:31:56 H	S17W24	542	527	530	-1.4	
3.	1998/05/01 – 23:40:09 H	S16W12	585	657	627	8	
4.	1998/04/29 – 16:58:54 H		1374	1151	1250	-44.8	
5.	1998/08/24 – 21:50	N35E09	--	--	--	--	1260
6.	1998/09/23 – 06:40	N18E09	--	--	--	--	1020
7.	1999/09/20 – 06:06:05 H	S20E01	604	549	357	-14.5	770
8.	1999/10/18 – 00:06:06 PH	S26E08	144	263	290	3.5	561
9.	2000/04/04 – 16:32:37 H	N18W72	1188	1232	1199	12.8	860
10.	2000/07/14 – 10:54:07 H	N17W11	1674	1534	1147	-96.1	1500
11.	2000/08/09 – 16:30:05 H	N11W15	703	731	720	2.8	830
12.	2000/09/16 – 05:18:14 H	N14W07	1215	1162	1192	-12.3	...
13.	2000/09/15 – 21:50:07 H		257	285	537	11.2	
14.	2000/09/15 –15:26:05 PH	N13W00	481	370	335	-10.4	
15.	2000/09/15 – 12:06:05 PH	N13W00	633	395	0	-64	
16.	2000/10/02 – 20:26:05 H	S09E04	569	478	483	7.1	756

17.	2000/11/03 – 18:26:06 H	N23W71	291	475	643	16.4	660
18.	2001/03/28 – 12:50:05 H	N17W03	519	582	561	4.4	690
19.	2001/03/29 – 10:26:05 H	N13W14	942	965	957	3.5	
20.	2001/04/10 – 05:30:00 H	S22W20	2411	2876	2974	211.6	1290
21.	2001/04/09 – 15:54:02 H	S21W08	1192	1198	1198	1.3	
22.	2001/09/29 – 11:54:05 PH	N14W01	509	470	150	-12	715
23.	2001/10/19 – 16:50:05 H	S14W62	901	895	898	-0.7	870
24.	2001/10/25 – 15:26:05 H	S19W26	1092	1080	1087	-1.4	694
25.	2001/10/24 – 06:26:05	S12E14	597	633	653	4.6	
26.	2001/11/04 – 16:35:06 H	N05W29	1810	1514	1691	-63.4	1250
27.	2001/11/03 – 19:20:05 H	N06W14	457	329	299	-9.9	
28.	2001/11/22 – 23:30:05 H	S18W24	1437	1371	1409	-12.9	1320
29.	2002/09/05 – 16:54:06 H	-	1748	1855	1903	43	880
30.	2002/09/26 – 01:31:44 PH	-	178	368	331	5.1	
31.	2003/10/28 – 11:30:05 H	S16E04	2459	2229	2268	-105.2	2185
32.	2003/10/29 – 20:54:05 H	S17W10	2029	1670	1519	-146.5	2138
33.	2003/11/18 – 08:50:05 H	N03E08	1660	1645	1656	-3.3	886
34.	2004/07/25 – 14:54:05 H	N08E35	1333	1366	1359	7	1302
35.	2004/11/04 – 23:30:05 PH	-	1055	1037	1050	-1.9	720
36.	2004/11/04 – 09:54:05 H	N09E32	653	719	706	6.3	
37.	2004/11/07 – 16:54:05 H	N09E08	1759	1696	1713	-19.7	830
38.	2004/11/06 – 02:06:05 PH	N09E06	1111	1258	1176	18.8	
39.	2005/05/13 – 17:12:05 H	N12E05	1689	--	--	--	1270
40.	2005/08/22 – 01:31:48 H	S11W54	1194	1086	1127	-17.8	790
41.	2005/08/22 – 17:30:05 H	S13W65	2378	2612	2585	108	
42.	2006/12/13 – 02:54:04 H	-	1774	1622	1573	-61.4	1180

The majority of active regions associated to coronal mass ejection have complex magnetic structure, like bipolar magnetic regions without a clear distinction between polarities, formed from several bipolar regions or magnetic regions in which the positive and negative polarity distribution is so irregular that they cannot be classified as bipolar regions.

The origin of coronal mass ejections can be located in a rectangle having as horizontal boundaries the longitudes -35 and 72, and vertical ones the latitudes 35 and -26.

The strongest geoeffective ejections – from October-November 2003 – have been located close to the centre of the Sun, had very high projected speeds values (1600-2460 km/s), and reached the Earth with high speeds.

1.1.3 Analysed Events

1.1.3.1. November 18, 2003

On November 18, 2003 a halo coronal mass ejection was registered, whose speed, calculated from the images offered by LASCO was of 1660 km/s. This ejection was produced by the eruption of a filament (Uralov et al., 2014), but also had a flare associated. The speed at the height of 20 solar radii was 1656 km/s, just 11 km/s less than the one registered at the final height of 28 solar radii, with a deceleration of just 3.3 m/s^2. The transit speed of this ejection at 1 AU was 886 km/s. The time between triggering of the ejection and the minimum Dst value moment was 59 hours, a lot longer than the time estimated using the projected speed – 25 hours.

Figure 1.1.1 shows the evolution of this ejection in LASCO white light images, superimposed on 195 Å EIT images. In the first frame, the solar flare associated with this eruptive event is visible in the EUV image. It was an M3.9-class flare above the active region NOAA 10501 (N03E08), very close to the disk centre. This flare started at 08:12 UT, had its maximum at 08:31 UT and ended at 08:59 UT, as the GOES X-ray data shows. In the same frame, but in the LASCO image, we can observe a coronal mass ejection that is still in development, which started ~45 minutes before the one we analyse here.

The ICME that followed this ejection was observed on November 20, at 08:03 UT and had a magnetic cloud associated.

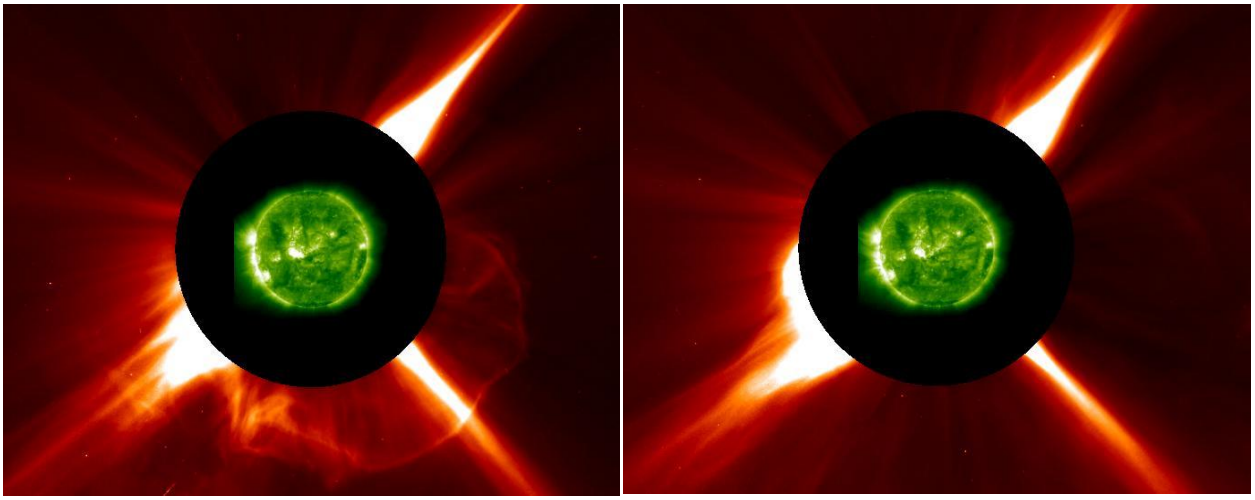

08:50 UT 09:48 UT

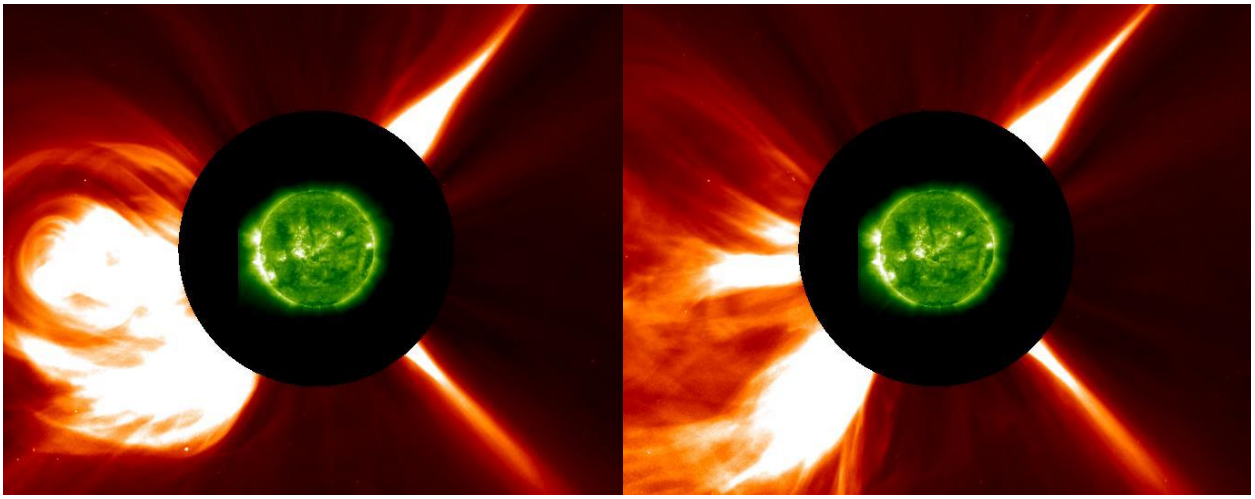

10:24 UT 10:48 UT

Figure 1.1.1 The evolution of the coronal mass ejection of November 18, 2003. Selected LASCO C2 images superimposed on solar disk 195 Å images provided by EIT. Composite images worked out with Jhelioviewer (jhelioviewer.org/)

1.1.3.2. November 7, 2004

A halo coronal mass ejection was registered by LASCO on November 7, 2004 at 16:54 UT. GOES registered an X 2.0 flare starting at 15:42 UT that had its maximum emission in X-ray at 16:06 UT and ended at 16:15 UT.

The flare was ignited in the active region NOAA 10696 situated at N09W22, a βγδ magnetic-type region. The active region where this flare ignited is shown in Figure

1.1.2, in running differences of EIT images on the last row, as compact structures that represent plasma with higher temperature than the surrounding lower corona.

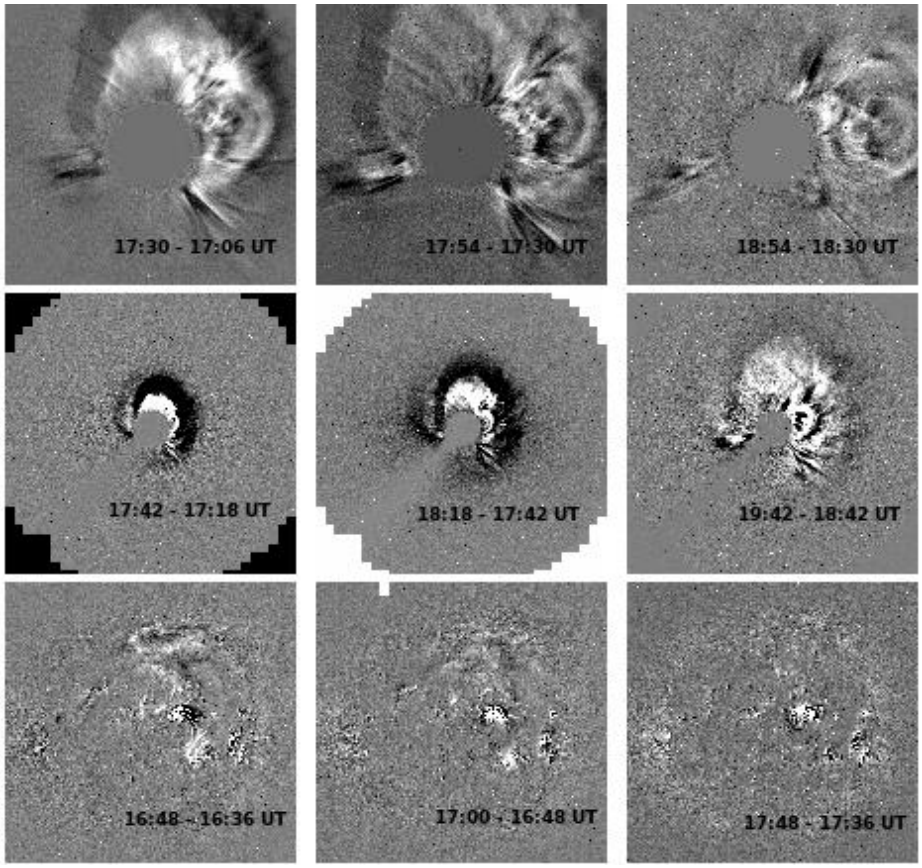

Figure 1.1.2: Selection of LASCO C2 running differences (first row), C3 (second row) and EIT (last row) showing the evolution of the November 7, 2004 CME.

The coronal mass ejection is visible in this Figure in the LASCO C2 images – in the first row – and those from LASCO C3, shown in the second row. The projected speed of this ejection was 1759 km/s, the final speed at the distance of 22 solar radii – 1969 km/s, and had a transit speed of 830 km/s. The acceleration for this CME was -19.7 m/s^2.

1.1.3.3. August 22, 2005

On August 22, 2005 LASCO detected a Halo coronal mass ejection at 01:31 UT. The solar flare registered by GOES was an M 2.6-type, whose X-ray flux begun to rise at 00:44 UT, had its maximum at 01:33 UT and came back to background level values at 02:18 UT. The flare was triggered in the active region NOAA 10798 (S11W62) whose

magnetic classification was βγ at that date. The location of the flare is visible in the last frame (lower right) of Figure 1.1.3.

This coronal mass ejection is visible in the Figure below in the LASCO C2 images (first row) and LASCO C3 (second row).

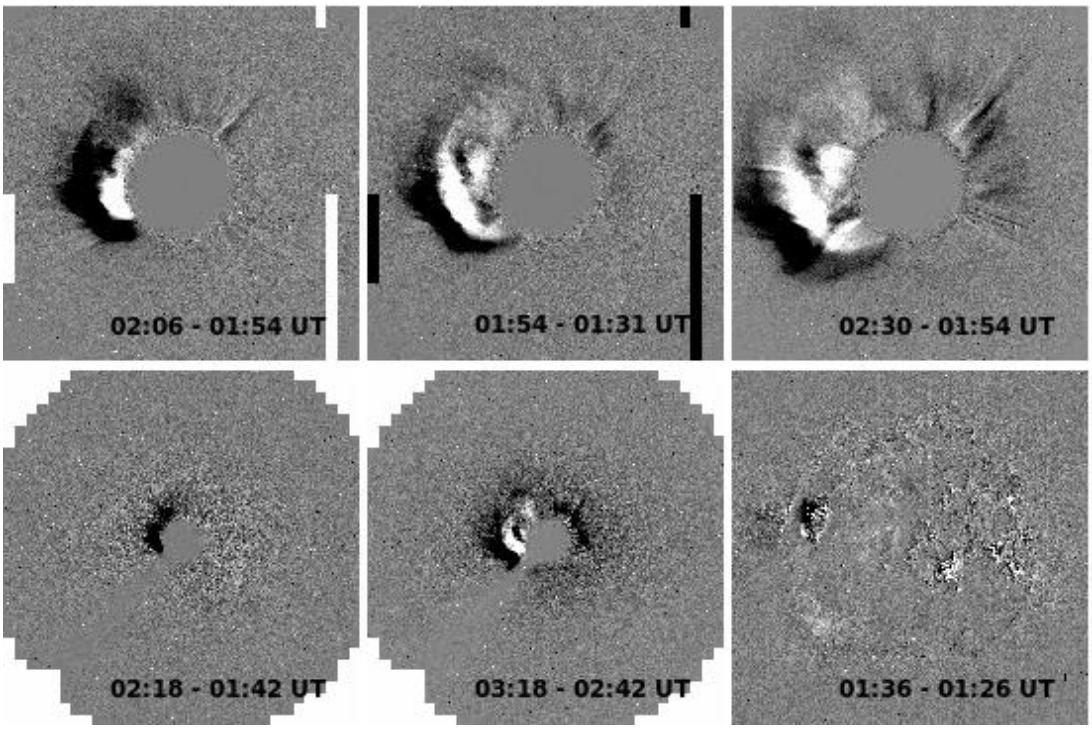

Figure 1.1.3: Running differences of LASCO C2 images (first row), LASCO C3 (second row first two columns), and EIT (last frame) showing the evolution of the eruptive phenomena of August 22, 2005.

This ejection was detected as an interplanetary one on August 24 at 02:38 UT and was accompanied by a magnetic cloud.

1.1.4. Modelling the geomagnetic efficiency of solar eruptive processes

Modelling the efficiency of an eruptive phenomenon is based on establishing some existing relations between the characteristic measurements of the analysed phenomena and their geoeffectiveness. It can refer both to the statistical evaluation of the number of coronal mass ejections and to the probability evaluation of producing a geomagnetic storm that follow certain coronal mass ejections.

The statistical evaluation of coronal mass ejections that are geoeffective is not representative in our case, because the number of ejections detected by LASCO is very

high (at the solar maximum activity there can be several CMEs/day), but the geomagnetic storms are much less.

The evaluation of the probability that a certain eruptive phenomenon be geoeffective is much more important. There are empirical models that evaluate this kind of probabilities. We chose as relevant data for the solar eruptive phenomena and the interplanetary coronal mass ejections the projected speed of the ejections at their detection in the LASCO images, the second order speed at different heights, the acceleration, the flare position on the solar disk, as well as two parameters of the interplanetary medium, the total magnetic field intensity and that of the southern component. However, this probability can give information only as what concerns major storms. A coronal mass ejection whose speed is not the highest as value, but is superimposed on an interplanetary magnetic field line whose direction is south, will be more geoeffective than a strong coronal mass ejection that reaches the Earth while Bz has negative values.

This study must be continued for the solar cycle 24 in order to benefit from the propagation speed direction of the coronal mass ejection at its triggering, with the help of several models based on the new satellite date from STEREO-COR2, relative to the solar wind direction at the analysed moment. Their positive superimposing will increase the probability of geoeffectiveness of the solar eruptive phenomenon.

1.2. The HSS contribution to major geomagnetic storms of the solar cycle 23

The solar wind, a continuous flux of plasma from the solar corona, is an inhomogeneous environment structured according to various parameters (density, plasma velocity, the heliospheric magnetic field structure). For this reason it is difficult to forecast its behaviour in the periterrestrial environment. However, certain structures, emitted and "controlled" by their solar sources, can be forecasted with a sufficient accuracy (70-95 %). The High Speed Streams (HSS), originating in Coronal Holes (CH) are a repetable structure and so forecastable. These streams produce, at the impact with the magnetosphere, average magnitude geomagnetic disturbances, but, in certain favorable circumstances (e. g., superposition to a sectorial boundary in the interplanetary space, the interaction with an ICME), they could produce important geomagnetic storms, they can significantly contribute to the development of magnetospheric currents at large scale. Their geoeffectivity is directly dependent on their solar source – the coronal hole – being influenced in the first place by the heliographic position of the latter. So, it is possible that CHs in the equatorial area or with

large extension to the equator produce HSSs with a major effect in the magnetosphere. Such CHs can be observed at the solar minimum or during the declining phase of the solar cycle. Also, HSSs emitted by a coronal hole are more geoeffective when the CH is close to the central meridian and during its passage through the western hemisphere. A HSS propagating from the solar corona through the interplanetary space interacts with the slow solar wind, forming at the boundary of the two flowing regimes a compression region, named Corotating Interaction Region, CIR), that often lives several solar rotations. Such structures appear because plasma is frozen in the magnetic field and the two streams (rapid and slow) do not mix, but form a persistent interface in their confluence zone. Consequently the properties of solar wind plasma and the structure of the interplanetary magnetic field are different in the two zones separated by the interface.

Table 1.2.1. Geomagnetic storms in the solar cycle 23 with HSS contribution

No	Date mm/dd/hh	Dst min (nT)	Bz min (nT)/Δt_{min}	Δt (h) (Bz<0)	B (nT)	SSC	Solar/Heliospheric Sources		
							CIR	Flare	CME/ICME
1999									
1	09/22/23	-173	-15,8/-1h	4 h	11	SSC	CH [2] / CIR [1]	C2.8	CME/ICME [3]
2	10/22/06	-237	-30.7/-1h	8 h	20	SSC	CH [1] /CIR [1]	CIR [3]	CME/ICME
2000									
3	04/06/22	-287	-27.3/-1h	7 h	6	gradual	CIR [1]	F [2] /C9.7	CME/ICME [3]
4	10/05/13	-182	-17.5/-2h	3 h	6	SSC	CIR [1]	F [2] / ?	CME/ICME [3]
5	11/06/21	-159	-11.7/-6h	9 h	20	SSC	CH [2]	-	CME/MC [3]
2001									
6	10/03/14	-166	-20.9/-2h	9 h	12	SSC	CIR [1]	F [2] /M1.8	CME/MC [3]

1 – Cid, C. et all, 2004, *Sol. Physics* **223**, 231-24
2 – Maris O., Maris G., 2009, HSS Catalog, at: http://www.spacescience.ro/new1/HSS_Catalogue.html
3 – Zhang, J. et all, 2007, JGR 112, A10102, doi: 10.1029/2007JA01321

In Table 1.2.1 the geomagnetic storms of the solar cycle 23 to which HSSs contributed (as triggering factors and/or as energy sources) are indicated. The date at which the minimum of the storm occured, the Dst minimum, the Bz minimum / the time difference between the Bz and Dst minima, respectively the time span (in hours), the scalar B value at the storm minimum, type of the storm beginning (SSC – sudden commencement – or gradual) are given. The last three columns give information on the solar and heliospheric sources of fluxex producing the storm. Under the table references are indicated.

One can notice the strong dependence between the negative values of Bz and the minimum of Dst and the fact that the Bz minimum precedes the Dst minimum. The 3-9 hours persistance of negative values of Bz ensures an efficient energy transfer and augments the imporatnce of the geomagnetic storm. All these remarkable storms occured in the maximum phase of the solar cycle, so the main role in triggering them is of particle fluxes emitted by solar eruptive phenomena, such as flares and CMEs. This can be seen also from the Table.

In Table 1.2.2 the characteristics of HSSs contributing to geomagnetic storms included in Table 1.2.1. Data regarding HSSs and geomagnetic storms are taken from *The Complex Catalogue GSs_HSSs for the Solar Cycle 23*, worked out within the frame of the project HELIOTER/PN 2, 2007 – 2010 (Maris O. & Maris, G. 2010, Complex Catalogue: GSs-HSSs, 1996 – 2008; at: http://www.spacescience.ro/new1/GS_HSS Catalogue.html).

Table 1.2.2. Characteristics of HSS that contributed to major storms of the solar cycle 23 and of the corresponding storms

HSS Data										Geomagnetic Storm Data			
Y	**M**	**D**	**3-h**	**V0**	**VMax**	**Dur**	**ΔVM**	**IMF**	**Sol. Sou.**	**Bz**	**Dst_min**	**t**	**Type**
				Km/s	Km/s	days	Km/s			nT	nT	mm:dd:hh	
1999	9	22	3	355.7	595.0	4.0	239.3	-	CH	-15.8	-173	09:22:23	SSC
1999	10	20	7	328.0	670.7	7.6	342.7	+	CH	-30.7	-237	10:22:06	SSC
2000	4	6	4	364.0	615.7	5.5	251.7	-	F	-27.3	-287	04:06:22	Gradual
2000	10	5	1	367.0	523.0	2.9	156.0	-	F	-17.5	-182	10:05:13	SSC
2000	11	3	6	334.0	608.0	5.8	274.0	+	F	-11.7	-159	11:06:21	SSC
2001	9	25	7	373.3	680.3	11.0	307.0	+	F	-6.4	-102	09:26:01	SSC
2001	9	25	7							-5.5	-55	09:29:21	SSC
2001	9	25	7							-12.7	-148	10:01:08	SSC
2001	9	25	7							**-20.9**	**-166**	**10:03:14**	**SSC**

For all HSSs the maximum speed of about 600 km/s and velocity jumps, ΔVMax = VMax – Vo, of 157 km/s - 342 km/s. The streams produced by CHs, as well as the solar particle fluxes contributing to storms were equally distributed in sectors of the positive or negative polarityof the heliospheric field (three in each sector). A special case is that of the HSS of September 25, 2001. During the 11 disturbed days, fluxes of solar plasma from coronal holes, flares and coronal mass ejections have produced complex disturbances in the magnetosphere, materialised in a succession of three geomagnetic storms of average intensity, followed by a major one, as it can be seen from the last four lines of the Table 1.2.2.

1.3. Discussion

There is no direct correlation, nor a bijective one, between the characteristic measures of the CME and the intensity of the geomagnetic storms. The coronal mass ejection with the greatest linear speed was not followed by the most intense geomagnetic storm. Nor was the interplanetary coronal mass ejection that reached the Earth with the highest speed.

Of much more importance is the orientation of the magnetic field that has to be southward oriented in order to allow the reconnection that triggers the geomagnetic storms.

A comparative study of speed, direction and positions of the coronal mass ejections, can provide information about possible effects on Earth. The study will be continued in the 2015 stage of the project.

References

Brueckner G.E., Howard, R.A., Koomen, M.J., Korendyke, C.M., Michels, D.J., Moses, J.D., Socker, D. G., Dere, K.P., Lamy, P. L., Llebaria, A., Bout, M. V., Schwenn, R., Simnett, G. M., Bedford, D. K., Eyles, C. J. (1995), *The Large Angle Spectroscopic Coronagraph (LASCO),* Solar Physics, **162** (1-2), 357-402

Carrington, R.: 1859, MNRAS 20, 13

Jian, L.; Russell, C. T.; Luhmann, J. G.; Skoug, R. M. ”Properties of Interplanetary Coronal Mass Ejections at One AU During 1995 2004” SoPh 239, 393, 2006

Hodgson, R.: 1859, MNRAS 20, 15

Richardson and Cane:”Near-Earth Interplanetary Coronal Mass Ejections During Solar Cycle 23 (1996--2009): Catalog and Summary of Properties” 2010, Solar Physics

Rouillard, A.P., JASTP 73, 1201, 2011

J. Zhang, I. G. Richardson, D. F.Webb, N. Gopalswamy, E. Huttunen, J. C. Kasper, N. V. Nitta, W. Poomvises, B. J. Thompson, C.-C. Wu, S. Yashiro, and A. N. Zhukov: ”Solar and interplanetary sources of major geomagnetic storms (Dst 100 nT) during 1996–2005”, 2007, Journal of Geophysical Research, 112, A10102

Zurbuchen, Thomas H.; Richardson, Ian G., In-Situ Solar Wind and Magnetic Field Signatures of Interplanetary Coronal Mass Ejections, Space Science Reviews, 123, 31-43, 2006

Chapter II. New geomagnetic and magneto-telluric measurements in Romania

2.1. Geomagnetic measurements

The geomagnetic measurements were carried out at the 26 repeat stations of the so-called National Network for secular variation, as well as at the Surlari geomagnetic observatory. The field measurement campaign took place in the time interval 13.08-2.09.2014. In Fig. 2.1.1 the way the territory has been covered during this campaign is illustrated. The geographical coordinates of the network stations are given in Table 2.1.1.

Determinations of the horizontal component H, total field intensity F, magnetic declination D, and magnetic inclination I have been carried out. In parallel with the absolute measurements, recordings of the field evolution, through the four elements X, Y, Z, and F, have been carried out. A DI-Flux LEMI 024 theodolite, two QHM magnetometers, a Geometrics G-856 and a recording LEMI-18 fluxgate magnetometer have been deployed.

The determined values were corrected for the diurnal variation and reduced to the time of the first reading of the series of determinations stipulated in the measurement protocol, by means of continuous recordings provided by the Surlari geomagnetic observatory. Then the values were processed to obtain values for the middle of the year 2013 (the geomagnetic epoch 2013.5), having in view the delay of about one year that affects observatory annual mean values against which the field data are reduced. In Fig. 2.1.2 the maps of the geographical distribution of the geomagnetic elements H, Z, D, and F are presented, reduced to the epoch 2013.5 for which the necessary data from the Surlari geomagnetic observatory were the definitive ones.

Table 2.1.1. Geographic coordinates of repeat stations on the Romanian territory

No.	Station	Latitude (degrees)	Longitude (degrees)
1	Saveni	47.96593	26.88277
2	Livada	47.84867	23.13362
3	Radauti	47.82142	25.94800
4	Somcuta	47.49997	23.43900
5	Vaida	47.25157	21.98520
6	Bistrita	47.19485	24.48570
7	Varatec	47.15150	26.29175
8	Cluj-Faget	46.69750	23.54715
9	Husi	46.67880	28.00265
10	Chisineu-Cris	46.54443	21.53978
11	Bretcu	46.05767	26.35652
12	Lipova	46.05202	21.72387
13	Deva	45.85712	22.91722
14	Dumbravita	45.83292	21.29002
15	Selimbar	45.75188	24.18742
16	Stamora	45.28383	21.24357
17	Gropeni	45.08573	27.86850
18	Mizil	44.99238	26.37497
19	Herculane	44.92215	22.44942
20	Babadag	44.87207	28.76385
21	Costesti	44.65898	24.89332
22	Strehaia	44.61763	23.16890
23	Tonea	44.20200	27.41502
24	Alexandria	43.96683	25.36662
25	Sadova	43.89513	23.93970
26	Negru-Voda	43.82022	28.24305
27	*Surlari Geomagnetic Observatory (SUA)	44.68000	26.25330

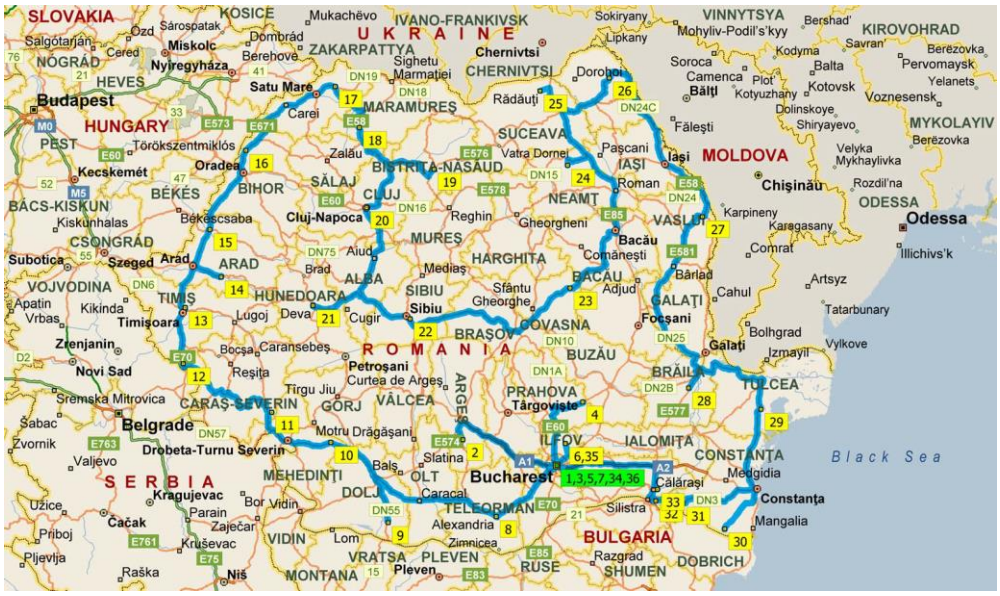

Fig. 2.1.1. The way the station network was covered in the time interval 13.08-2.09.2014

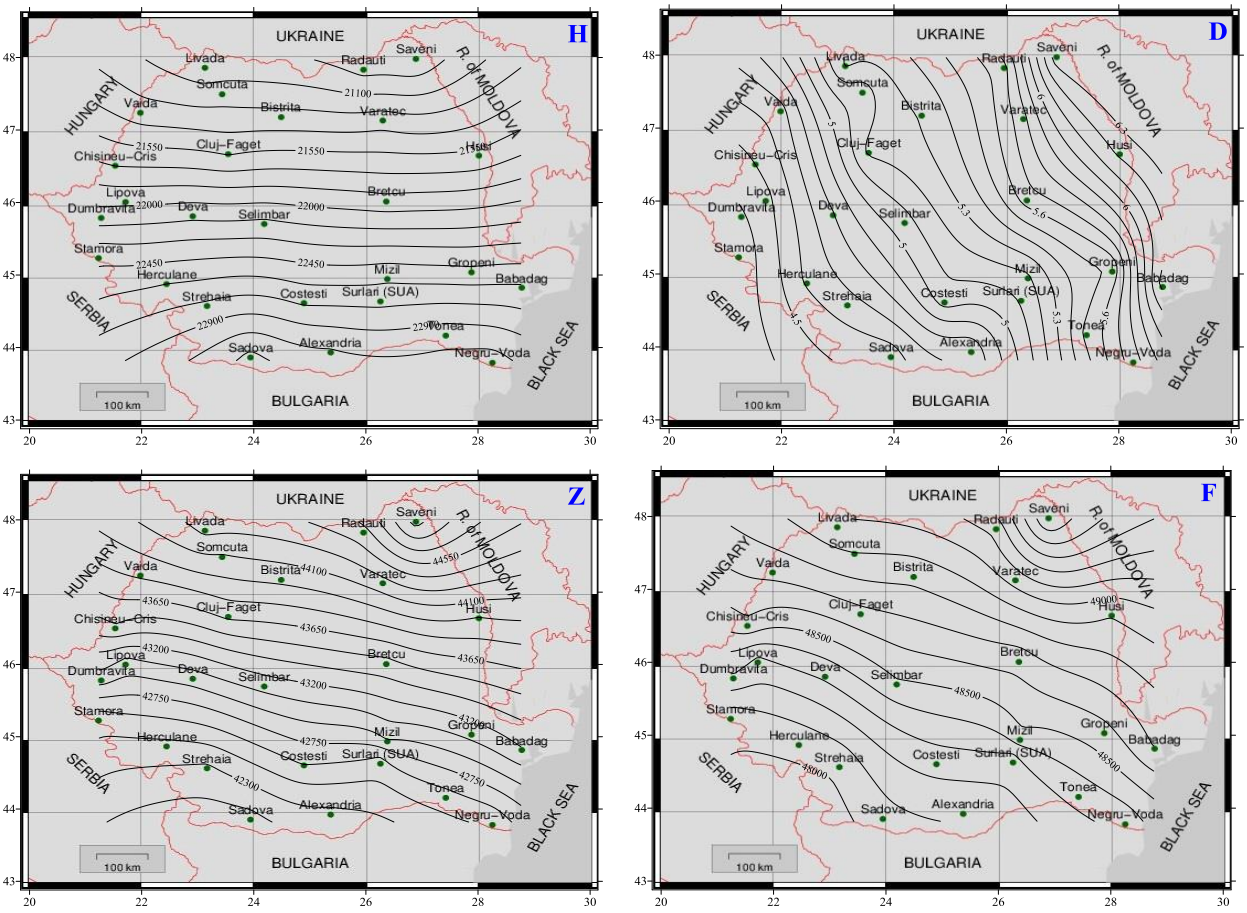

Fig. 2.1.2. The geographical distribution on the Romanian territory of the geomagnetic elements H, D, Z, and F at epoch 2013.5 (measurements carried out in 2014). The repeat stations of the National secular variation network are marked by symbols

2.2. Magneto-telluric measurements

In the second part of September and in the beginning of October 2014, two magnetotelluric soundings (MTS), located close to Ludus and, respectively, Bazna (Fig.1) have been carried out in the Transylvanian Depression. In order to obtain very low frequencies able to investigate the crystalline basement, that is situated in the investigated area at depths of 7-8 km, the recording time of the EM series (Ex, Ey, Bx, By and Bz) was of about 10 days. Thus the frequency range used was between 10^{3} Hz and 10^{-4} Hz.

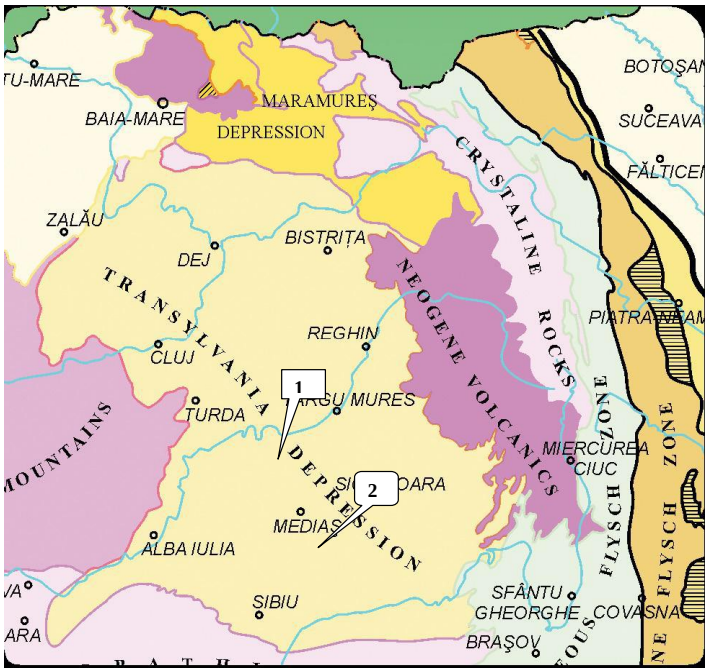

Fig. 2.2.1. Location map for the two mageto-telluric (MT) stations in the Transylvanian Basin: MTS Luduş (46 : 28; 47.81), altitude 368 m (1); MTS Bazna, (46 : 11; 40.52), altitude 355 m (2)

2.2.1. The geology and the lithology of the studied area

The Transylvanian Basin is characterized by a sedimentary cover of 1200 - 8000 m, thinner in the northern part and thicker in the vicinity of the Mures river. The basin includes the following sedimentary cycles: Upper Cretaceous, Paleogene, Burdigalian-Helvetian, Tortonian-Buglovian-Sarmatian, Pliocene, and Quaternary.

As regards the crystalline basement of the basin, in its composition there are epimethamorphic (to East) and mesomethamorphic (to West) schists, that were intercepted by drillings at various depths, covered by Mesosoic deposits (conglomerates, limestones) having an epicontinental character (intercepted only in a few places). The tectonic

movements at the end of Cretaceous and in Paleogene fragmented the crystalline block in subunits that, in Lower Paleogene - Miocene, underwent week subsidence and even uplifts. From the midle Miocene all of them subsided with different intensities. This had some consequences as regards the level of the basement blocks: three more elevated compartments may be distinguished (Paucă, 1972, V.Mutihac, 1990): (1) Blaj-Pogăceaua at 3000 m; (2) Făgăraş–Perşani at 1200 – 3000 m; (3) The Somes – Prisnel up to 2000 m, separated by three deeper compartments: (i) Turda–Beclean at 6000 m; (ii) Tarnava rivers compartment at 8000 m; (iii) Odorhei–Deva at 6500 m. The Dej tuff was intercepted at the basin margin, with a thickness of 10-500 m.

2.2.2. Processing, modelling, and 1-D inversion of resistivity curves. Methodology

A multi-channel magnetotelluric system (GMS-06) produced by METRONIX company, Germany, was used. The central unit ADU-06 has 5 channels at which 4 un-polarized sensors for electric field recording and 3 magnetic sensors (induction coil) for magnetic field recording are connected. The frequency range recorded was 10^{3}-10^{-4} Hz. Data are stored on the internal "flash disk" or directly on the computer HDD, on which the MAPROS program is installed. This program operates under Windows 95 and takes the control over the following operations:

1. Semi-automatic settings in field of the electric and magnetic sensors;
2. Real-time data acquisition and processing;
3. Robust estimation of the magnetotelluric transfer functions Zxy, Zyx and of the geomagnetic transfer functions Txy ,Tyx;
4. Real-time time series representation for MTS Bazna (Fig. 2.2.2) and for resistivity and phase curves for MTS Ludus (Fig. 2.2.3) and MTS Bazna (Fig. 2.2.4).

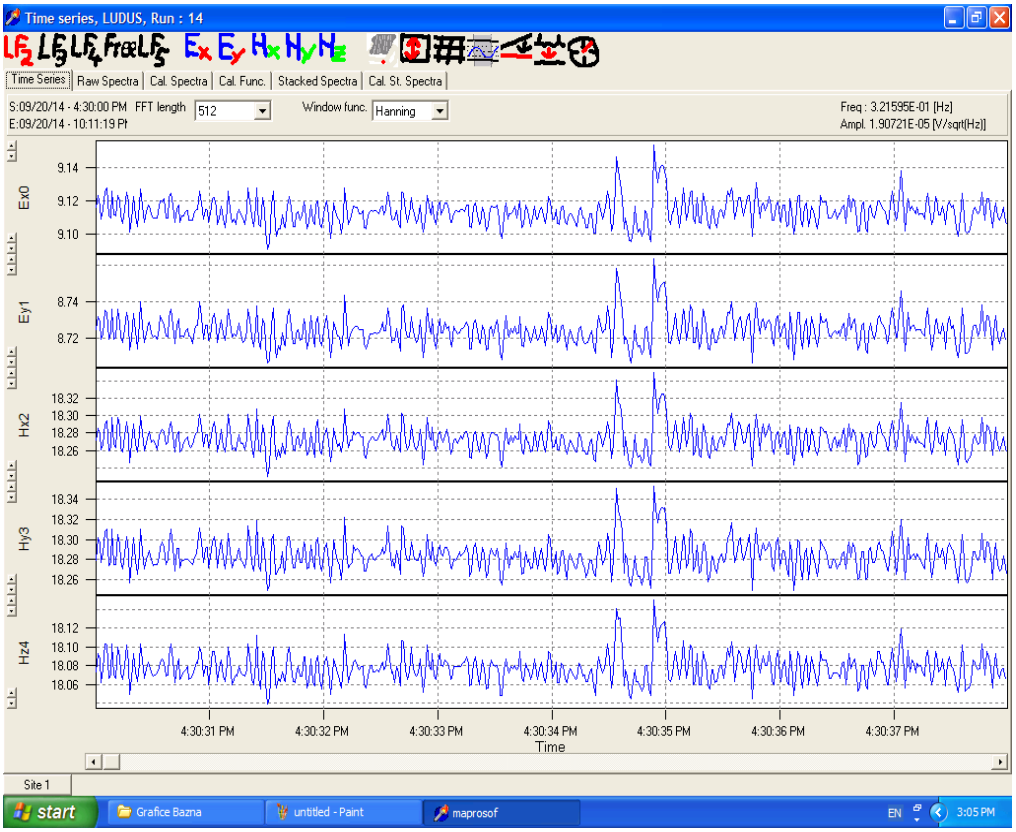

Fig. 2.2.2. Magnetotelluric time series: electric components (Ex, Ey) and magnetic components (Bx, By, Bz) for MTS Bazna

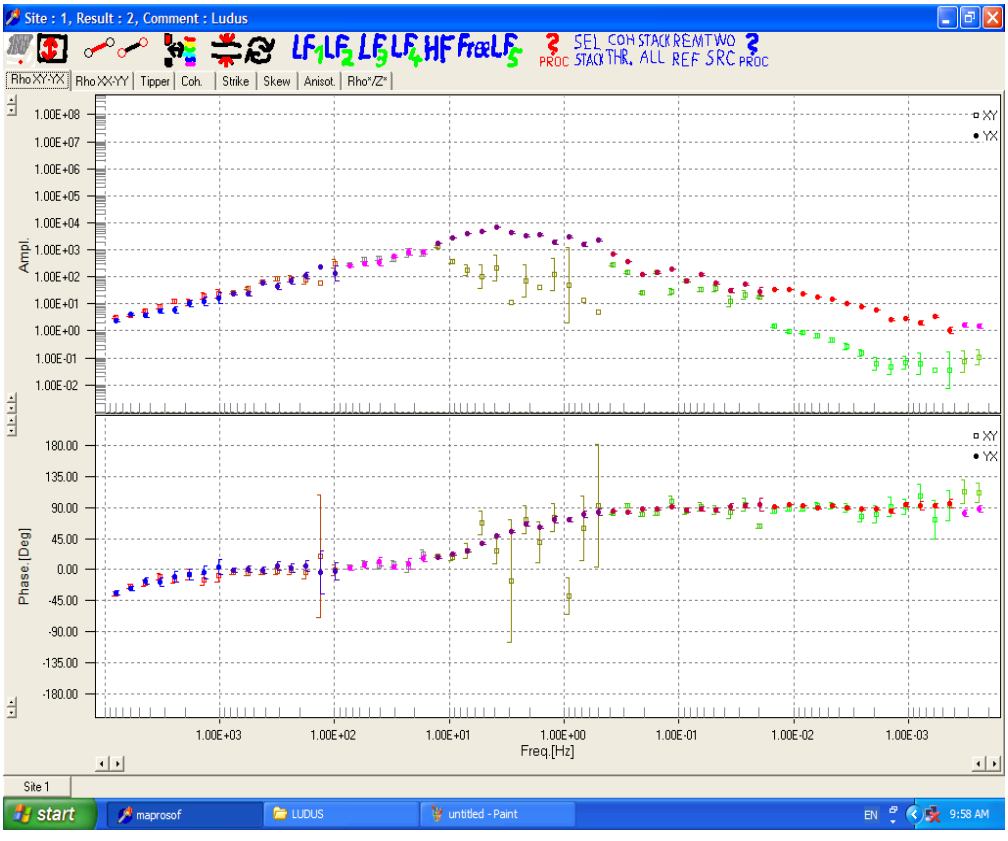

Fig. 2.2.3. Resistivity (upper plot) and phase (lower plot) distributions versus frequency for MTS Ludus

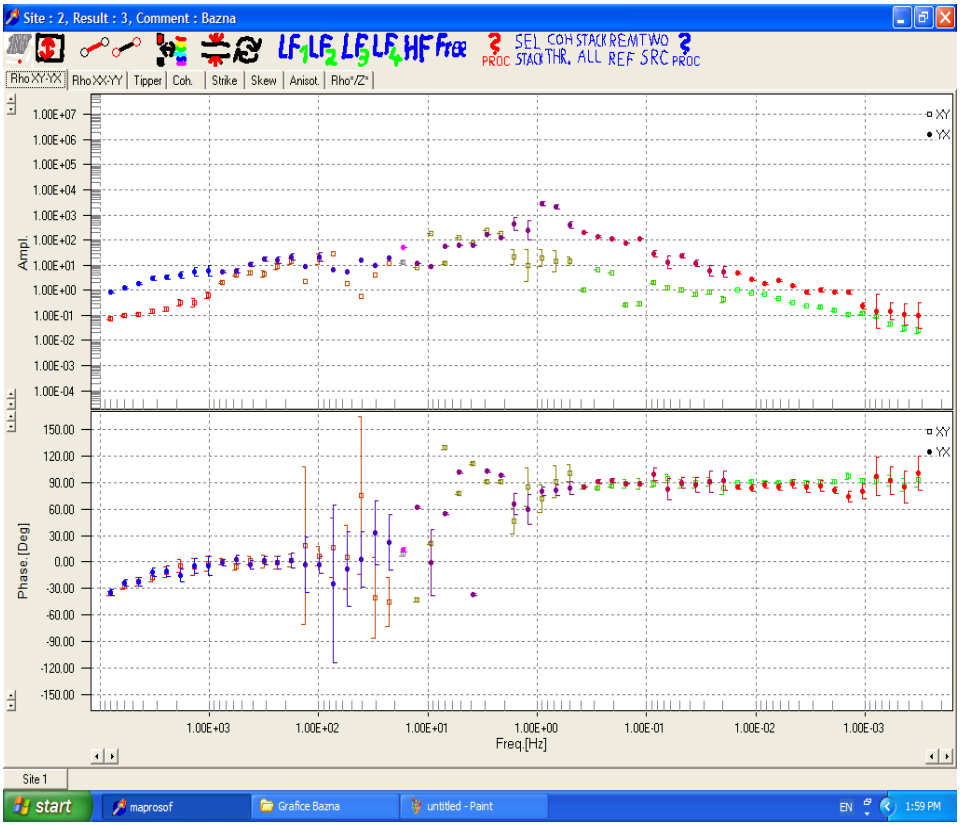

Fig. 2.2.4. Resistivity (upper plot) and phase (lower plot) as a function of frequency for the MTS Bazna

As regards the vertical distribution of the resistivity obtained for the two MTS, we have to mention that these were achieved by using a 1-D inversion program. The results are presented as 1-D models in Fig. 2.2.5 for MTS Ludus and in Fig. 2.2.6 for MTS Bazna. These results reflect the resistivity distribution from the Earth's surface down to the crystalline basement.

The models represent the most probable images as compared to reality, because between the computed response functions and the experimental values there is a deviation of at most 2%. According to "Legend" attached to figures, the models for the sedimentary cover show thicknesses of 6.8 km (MTS Ludus) and 8.5 km (MTS Bazna), and resistivities of about 2-10 Ωm. The resistivity of crystalline basement is between 700 Ωm and 1000 Ωm. This information adds to the one obtained previously (Stages 2012 and 2013) based on magneto-telluric soundings in the data base of the project, contributing the resistivity model for the main crustal blocks presented in the following.

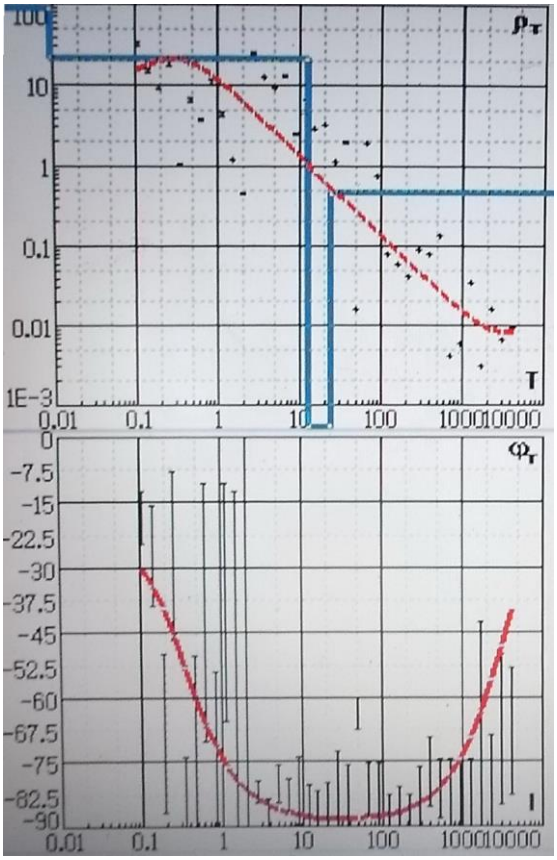

a.

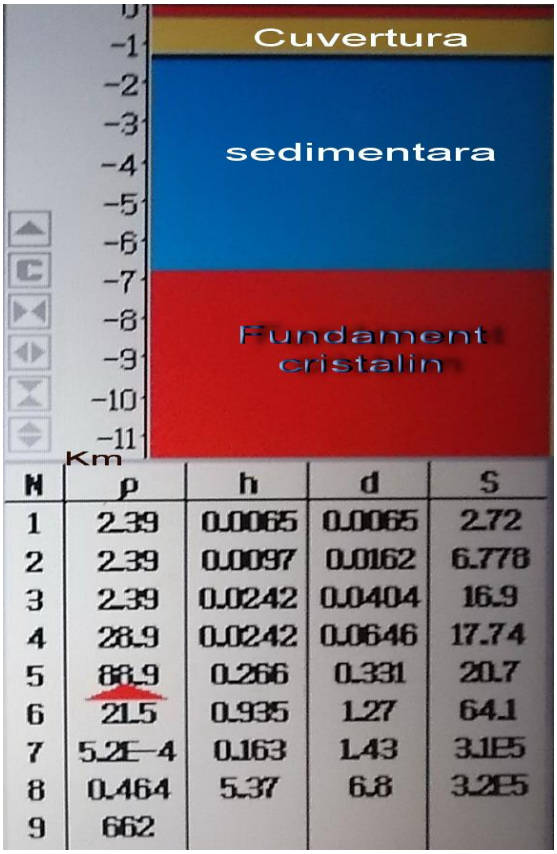

N	ρ	h	d	S
1	2.39	0.0065	0.0065	2.72
2	2.39	0.0097	0.0162	6.778
3	2.39	0.0242	0.0404	16.9
4	28.9	0.0242	0.0646	17.74
5	88.9	0.266	0.331	20.7
6	21.5	0.935	1.27	64.1
7	5.2E-4	0.163	1.43	3.1E5
8	0.464	5.37	6.8	3.2E5
9	662			

b.

Fig. 2.2.5. 1-D modelling for MTS Ludus. Resistivity and phase curves (a), 1-D model (b) (N-number of layers, ρ- apparent resistivity, h- thickness of layer , d- depth, S-conductance)

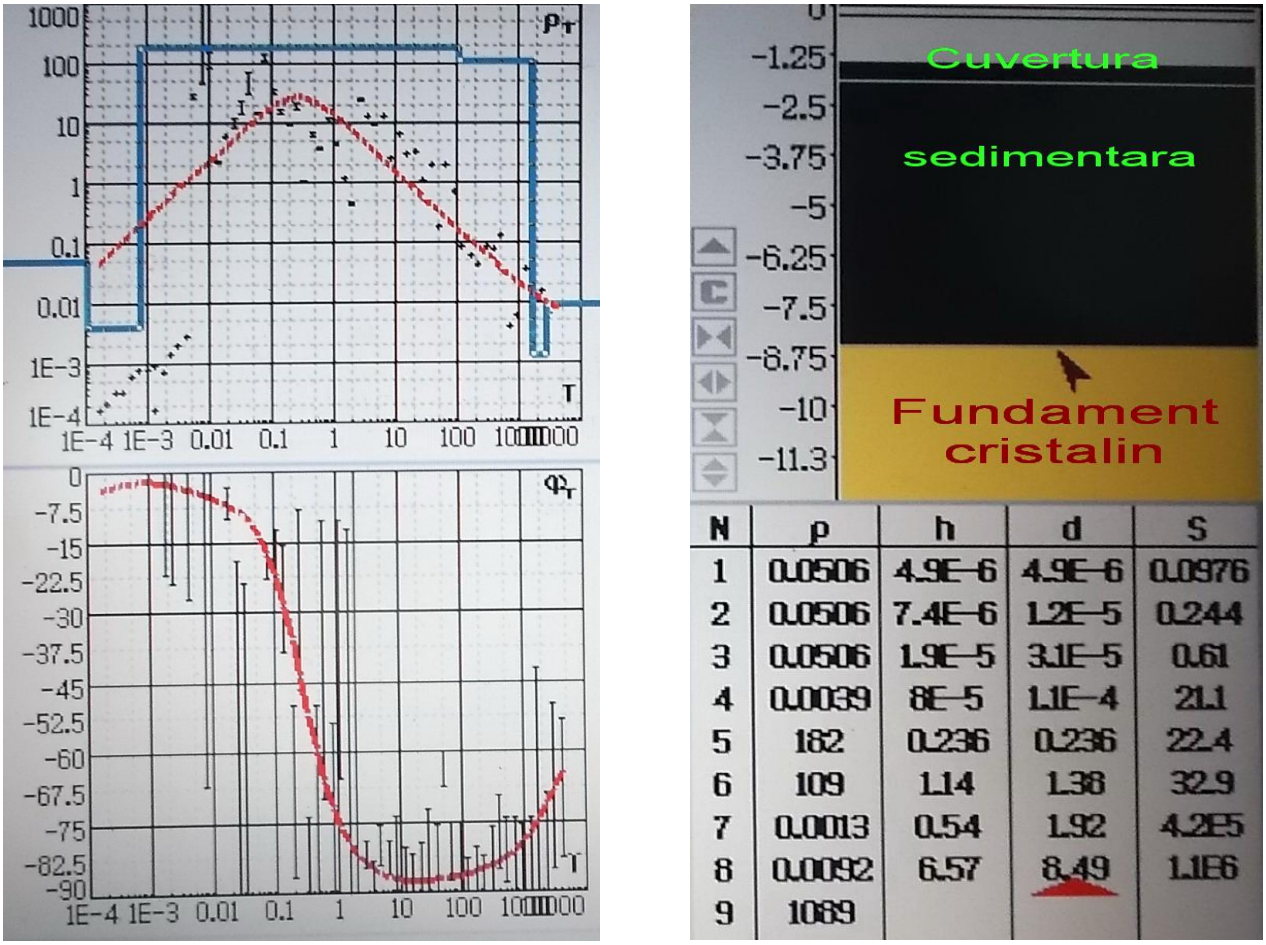

a. b.

Fig. 2.2.6. 1-D modeling for MTS Bazna. Resistivity and phase curves (a), 1-D model (b) (N-number of layers, ρ- apparent resistivity, h- thickness of layer , d- depth, S-conductance)

Chapter III. Magnetic and electric structure of terrestrial litosphere and mantle at Romanian territory and continental scales. 3D model of the electric resistivity distribution on the Romanian territory

3.1. Model at the European continental scale, based on analysis of intense geomagnetic storms in solar cycle no. 23

In the previous stage report (year 2013) we presented an application of the so-called „magnetic and electromagnetic induction mehod", previously worked out by the contract team members, to the case of a major geomagnetic storm (15.05.2005). In the present stage we extended the study to a number of storms, in order to assess the robustness of the result to variations of the inducing force.

3.1.1. The principle of the metod and data used

The method used in the present work (see the Phase 2013 report) is based on the observation that an external variable field induces inside the Earth variable magnetic fields not only through electromagnetic induction in conductive structures of the crust and mantle, but also by magnetic induction in rocks above the Curie temperature. In the pure magnetic induction case, the temporal variation of the field components at a certain observation point is given by a linear combination of the components of the inducing magnetic force. The calculated values of the model represent the component of the observed signal produced by pure magnetic induction, while the residuals contain the information related to the electromagnetic induction in the Earth at the given point. The model coefficients can be determined by a least squares procedure and mapped, resulting in images of the lateral (geographical) distribution of magnetic properties that characterise the rock volume above the Curie temperature (generaly the crust).

In case of **electric properties** of crust and mantle, the residual of the induction model for the **vertical component of the field** is used. The latter responds to the electromagnetic induction in the electrically conducting crustal and mantle structures to a greater extent than the horizontal component. As the induction electromotive force is given by the negative time derivative of the inducing magnetic field, the latter should correlate with the observed residual. The working relationship is:

$$-\dot{Z}_{sursa}(t) = L \cdot \dot{Z}rez(t) + R \cdot Zrez(t),$$

where $-\dot{Z}_{sursa}$ is the negative time derivative of the vertical component produced by the inducing source, and Zrez is the residual of the induction model applied to the Z component recorded at the observation point. L and R, the electrical inductance and, respectively, the resistance that characterise the crust and mantle under the given observatory, can be determined for each observatory by means of the least squares method, for the given time interval. Mapping of the obtained values reflects the lateral distribution of the Earth interior electric properties. The mapped values are relative, the maps reflecting, as was also the case of magnetic properties of the crust (the 2012 Report), lateral variations of the parameters L and R, not real (absolute) values. Also, the obtained information regards a large depth range, from the surface to mantle depths.

The magnetic storms illustrated by means of the Dst index in Fig. 3.1.1 were used. For each case the available recordings on the INTERMAGNET site www.intermagnet.org. (minute values) 12 hours long, including the storm, were downloaded. The external source is represented by variations of the magnetospheric ring current through the geomagnetic index Dst (minute values) provided by the site http://geomag.usgs.gov/data. The Dst index represents the effect of the ring current at the Earth's surface, in the geomagnetic equatorial area.

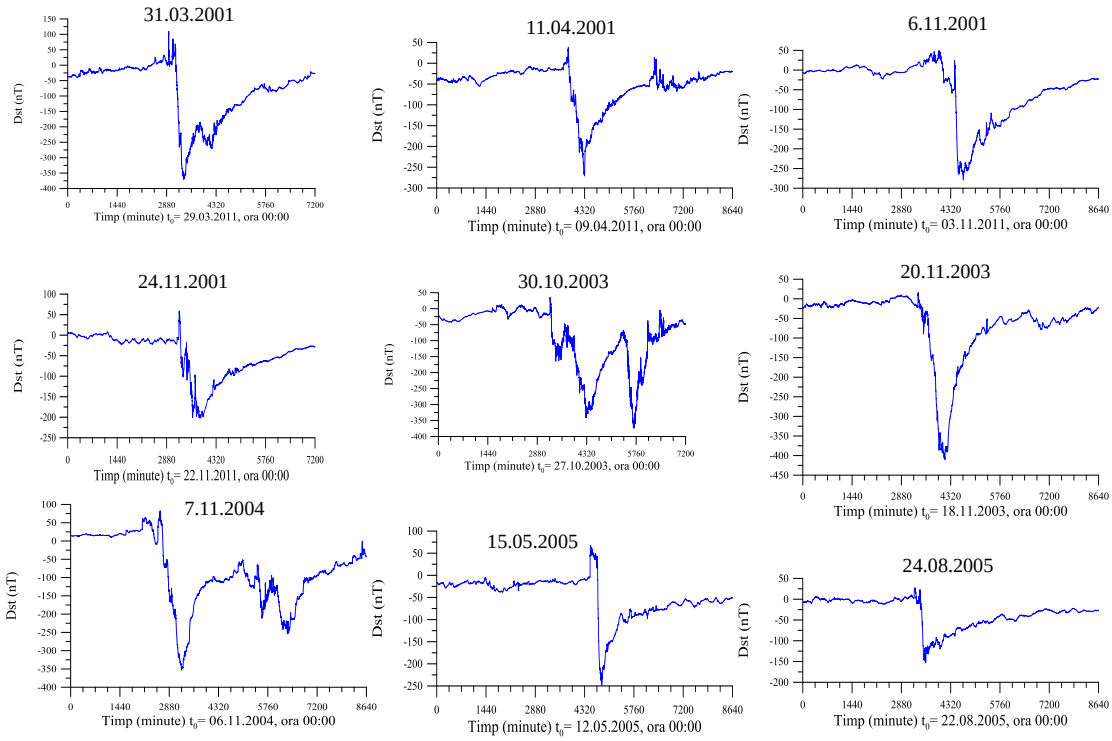

Fig. 3.1.1. The variation of the Dst geomagnetic index for the analysed geomagnetic storms

3.1.2. Results

In Fig. 3.1.2 we give the results for each of the analysed storms as regards the electrical resistence (the parameter of interest in modeling the surface electric field produced by variations of the geomagnetic field). A first observation concerns the fact that the distribution of observatories providing data is not the same in all cases, making difficult a correct comparison of results. In Fig. 3.1.3 we show maps with the same distribution of observatories in all of them. One can see that, in general, the distribution of the electric resistence is similar, with lower values in the southern and south-western part of the network than in the north-eastern part. Of course, local differences, still visible, could be put on the different morphology of the considered geomagnetic variations (an evident case is that of the

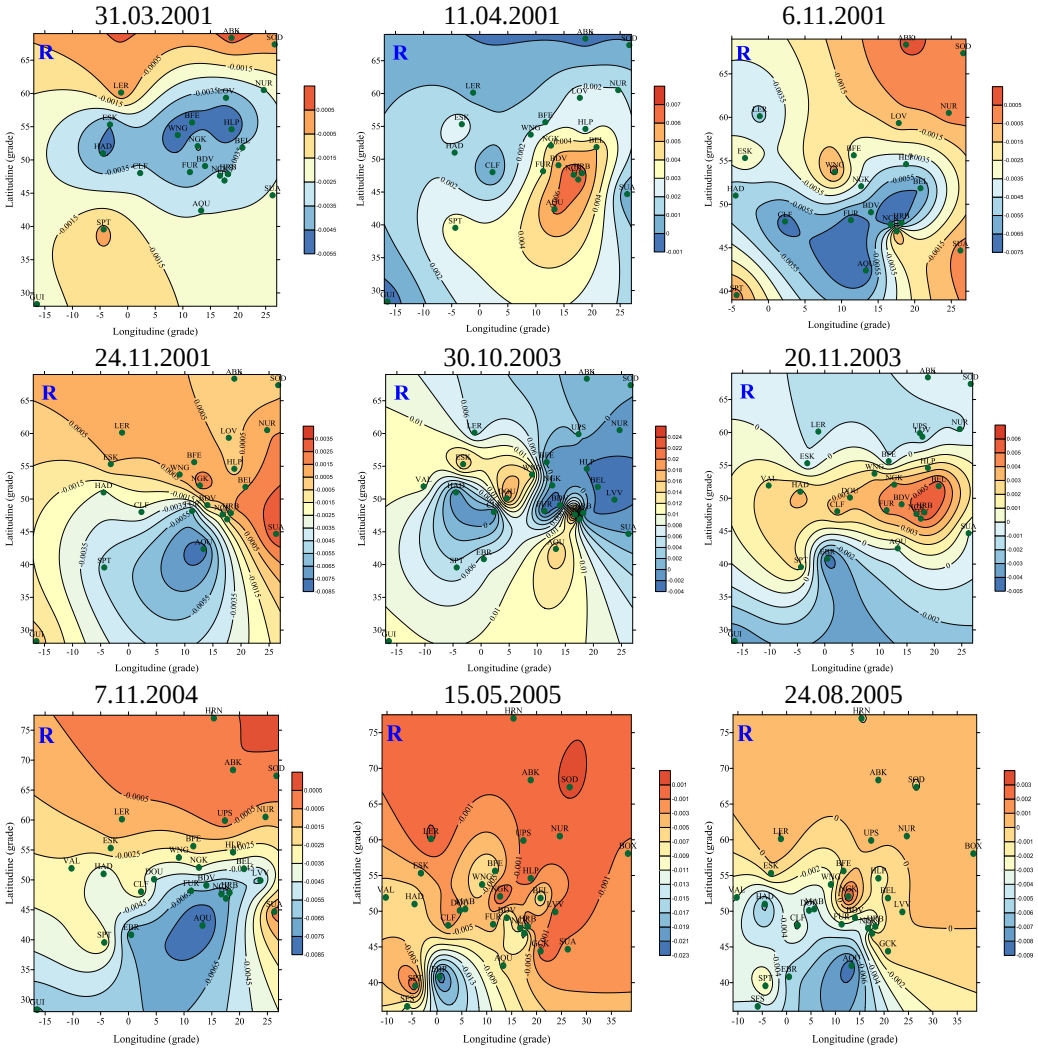

Fig. 3.1.2. Maps of the distribution of the electrical resistance at the European continental scale for the major storms marked on the figure

30.10.2003 storm), with consequences in the first place regarding the penetration depth in the Earth. To elucidate this aspect, we shall tackle in the next stage of the contract the study of only the main phase of the storm.

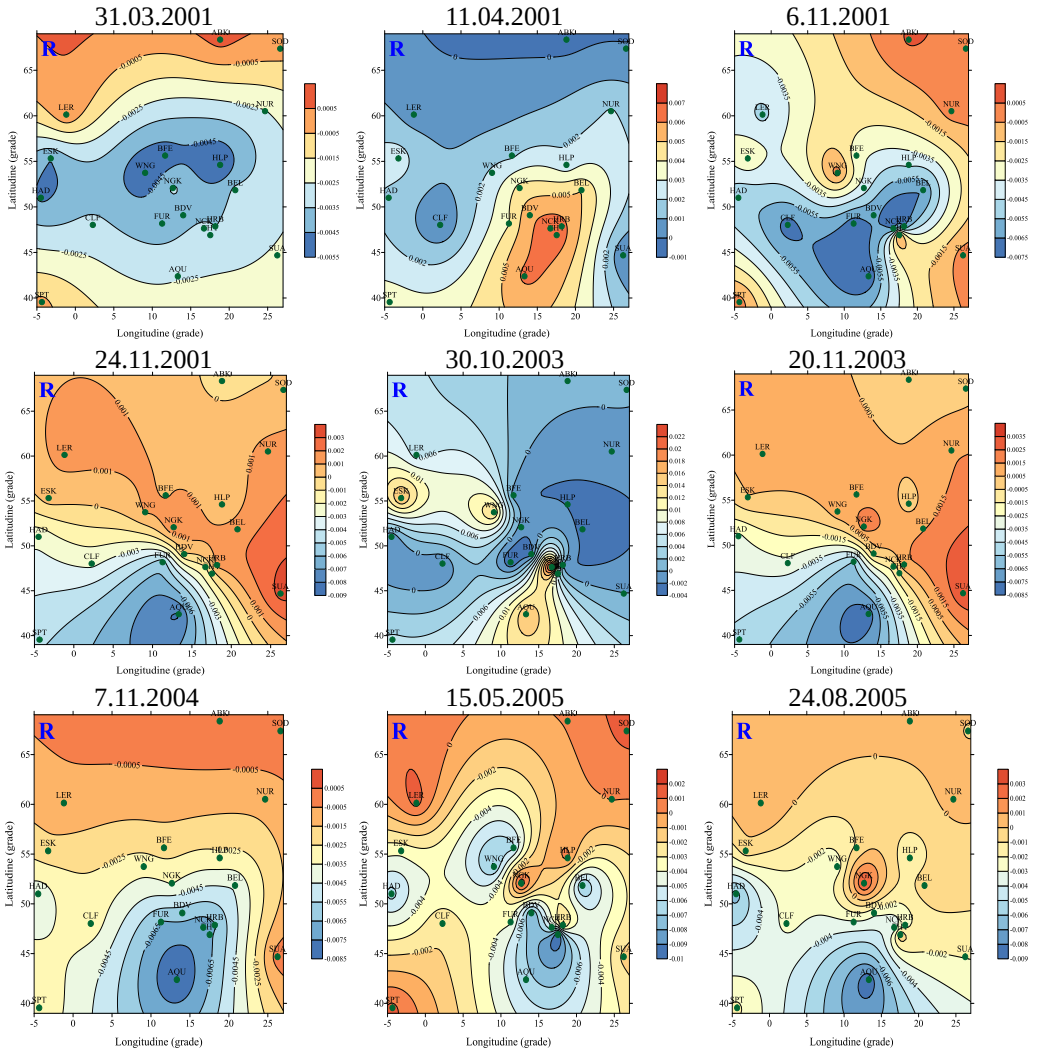

Fig. 3.1.3. Maps of the distribution of the electrical resistance at the European continental scale for the major storms marked on the figure, in case the observatory distribution is the same in all six maps

3.2. Model at national territory scale, based on magneto-telluric research carried out within the frame of the contract

In the present phase of the contract we present a quasi-3D model of the resistivity distribution on the Romanian territory, that follow the geological block structure that form the terrestrial crust on the study area. Each main block has a stratified electric structure, as determined by means of the results for the numerous magneto-telluric deep soundings profiles of the project data base (see Fig. 3.2.1), discussed in previous stages. The following

major tectonic units were in view: the East-European Platform, the Transylvanian Depression, the Pannonian Depression and the Moesian Platform. Models are schematically presented in the next section. To these, a discussion on the Carpathian Electric Conductivity Anomaly (CECA) is added.

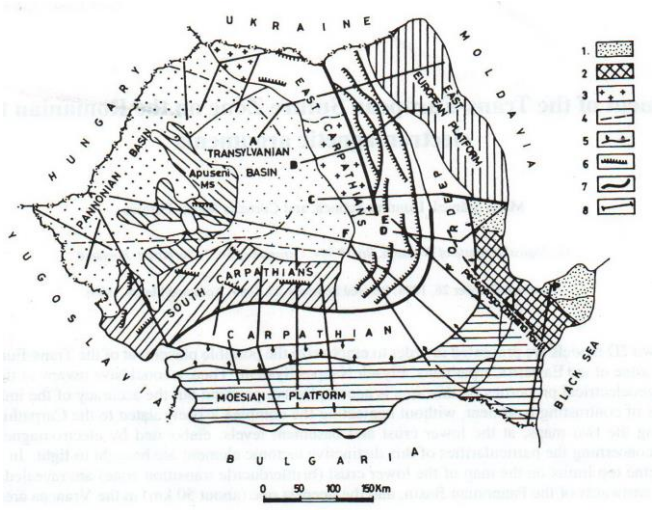

Fig. 3.2.1. Map of magneto-telluric geotraverses on the Romanian territory (after Stanica et al., 1999). 1- Scytian Platform; 2 - North Dobrogean Orogen; 3 - Neogene volcanic chain; 4 - deep fault; 5 - flexure; 6 - overthrust; 7 - CECA; 8 - MT profile

3.2.1. Resistivity litospheric model representative for the East-European Platform

Platforma Est-Europeană
Model1D de distribuție a rezistivității (ρ) în litosferă

Strate	ρ[Ωm]	h[km]	Observații
1	10	10	Cuvertură sedimentară de platformă
2	1000	30	crustă
3	10	10	zonă de tranziție de la crusă la mantaua superioară
4	500	130	Mantaua superioară
5	10		Astenosfera

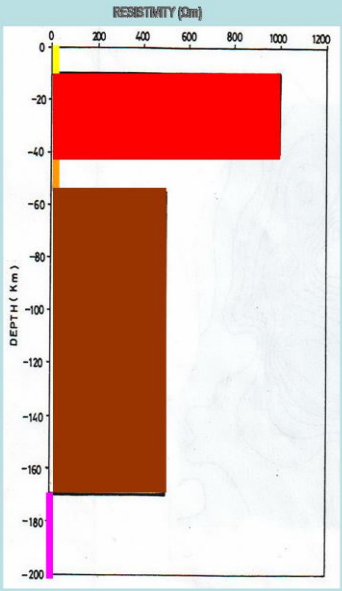

3.2.2. Resistivity litospheric model representative for the Transylvanian Depression

Depresiunea Transilvaniei

Model1D de distribuție a rezistivității (ρ) în litosferă

Strate	ρ[Ωm]	h[km]	Observații
1	5	4	Cuvertura sedimentară post-tectogenetică
2	500	2	Pânzele Central-Est Carpatice-subasment cristalin
3	700	24	Crusta
4	10	10	Zona de tranziție de la crusta inferioară la manta
5	500	40	Mantaua superioară
6	10		Astenosfera

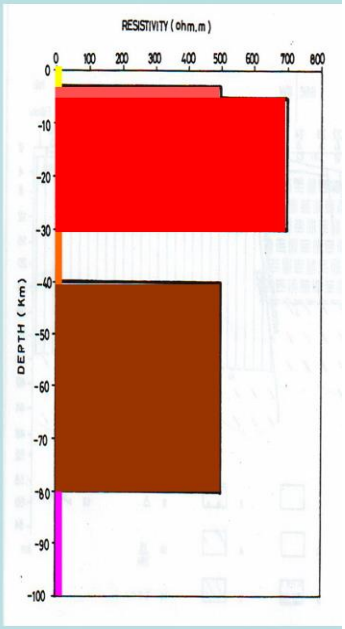

3.2.3. Resistivity litospheric model representative for the Pannonian Depression

Depresiunea Pannonică

Model1D de distribuție a rezistivității (ρ) în litosferă

Strate	ρ[Ωm]	h[km]	Observații
1	5	4	Cuvertura sedimentară
2	700	16	crusta
3	10	10	Zonă de tranziție crustă-manta
4	500	30	Mantaua superioară
5	10		Astenosfera

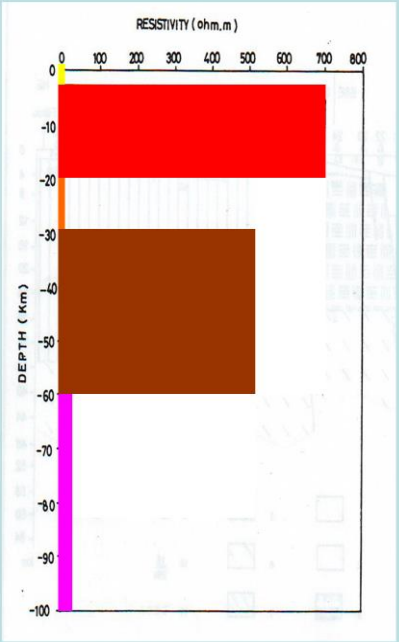

3.2.4. Resistivity litospheric model representative for the Moesian Platform

Platforma Moesică

Model1D de distribuție a rezistivității (ρ) în litosferă

Strate	ρ[Ωm]	h[km]	Observații
1	10	10	Cuvertură sedimentară de platformă
2	1000	30	crustă
3	10	10	zonă de tranziție de la crusă la mantaua superioară
4	500	80	Mantaua superioară
5	10		Astenosfera

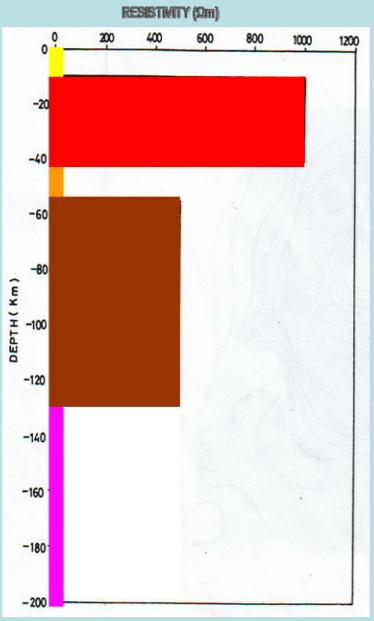

3.2.5. The Carpathian Electric Conductivity Anomaly (CECA) in Romania, structural peculiarities

To show the most important electrical conductivity anomaly in Romania, the Wiese induction vectors map (Pinna et al.1992) and the results of the deep MT soundings (Stănică et al., 1999) were used. As it may be seen in Fig.3.2.2, CECA may be correlated with the alignment of the Wiese induction vectors divergence zone. It is developed vertically at the contact between two types of crust with different thicknesses and electrical properties (East-European/ Transylvanian) but also within the Moesian crust.

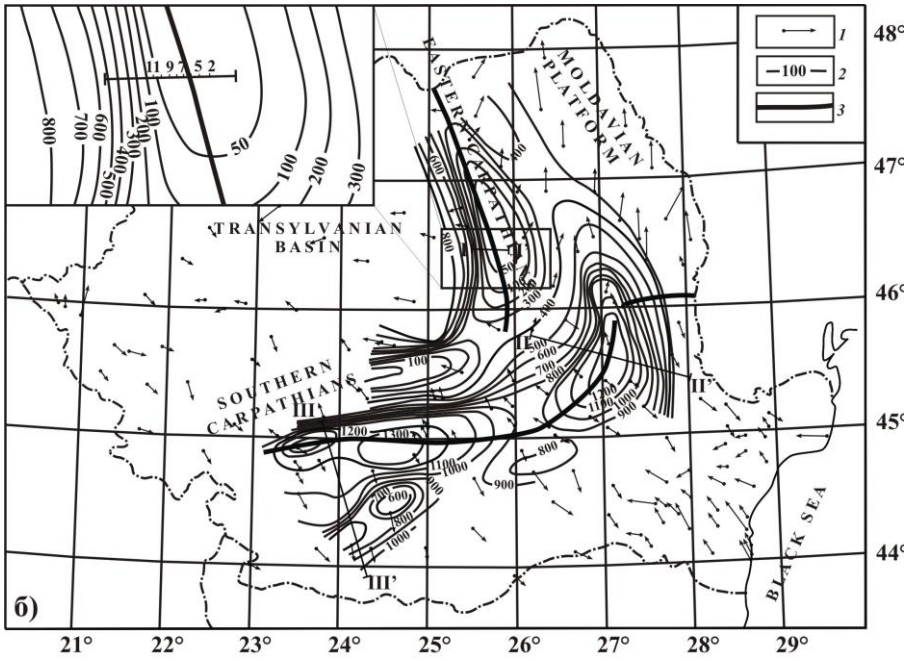

Fig. 3.2.2. Wiese induction vectors for periods of 5-50 s (1), total longitudinal conductance isolines for the sedimentary cover according to data from MTS geotraverses (2), CECA axis (3) (after Pinna et al., 1992).

In the upper left hand side of Fig. 3.2.2 a detail of the rectangle in the same figure that includes the profile I-I' with soundings from the central CECA is given. The obtained information shows:

1. A horizontal extension of about 20 km;
2. Its upper part is approximately at 10 km under the flisch nappes;
3. The vertical development is estimated to at least the crust base.

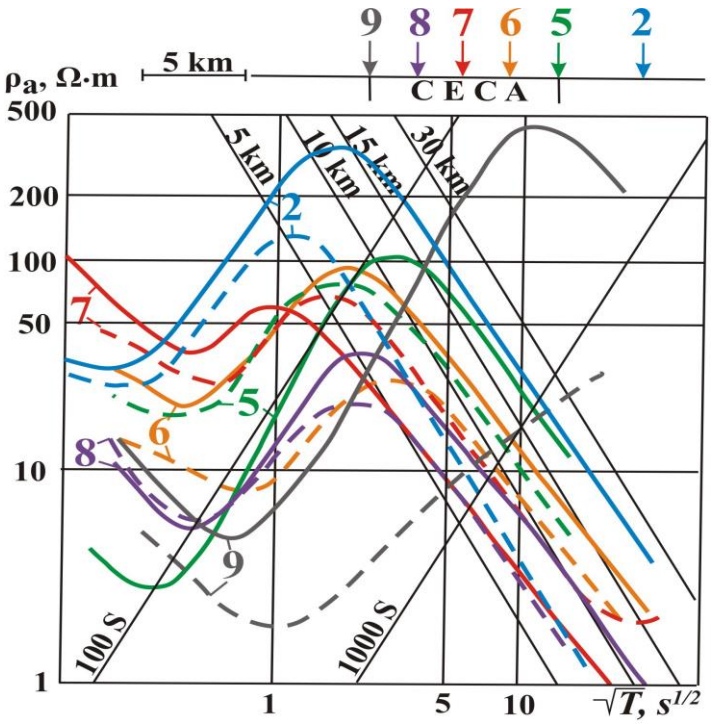

Fig. 3.2.3. MTS curves for the CECA central zone. Full and dashed colored lines show perpendicular and, respectively, parallel to CECA resistivities, numbers 2, 5, 6, 7, 8 and 9 correspond MTSs (after Pinna et al., 1992)

In Fig. 3.2.4 a 2-D model for the resistivity distribution is presented for the profile II-II' of Fig. 3.2.2, located in the bend zone of the Eastern Carpathians were CECA shows:

1. A horizontal extension of about 8 km;
2. Its upper part is at approximately 15 km under the flisch nappes and a part of the platform sedimentary cover;
3. A vertical development to the crust base (approx. 45 km).

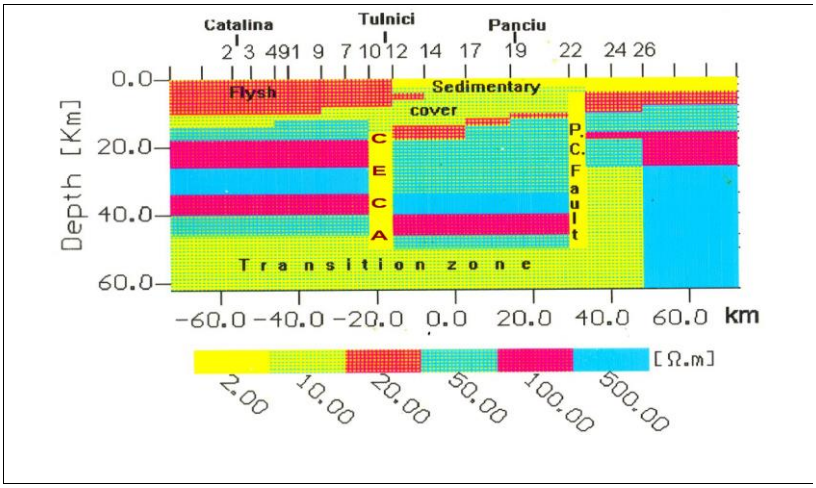

Fig. 3.2.4. 2-D Model for the resistivity distribution along the II-II' profile in the bending zone of the Eastern Carpathians

In Fig. 3.2.5 a 2-D model is presented for the resistivity along the profile III-III' of Fig. 3.2.2, crossing the Southern Carpathians, Carpathian foredeep and the northern part of the Moesian Platform. CECA shows the following characteristics:

1. A horizontal extension of about 6 km;
2. Its upper part is placed approximately 10 km under the flisch nappes and a part of the platform sedimentary cover;
3. Vertical displacement to the base of crust (approx. 30 km).

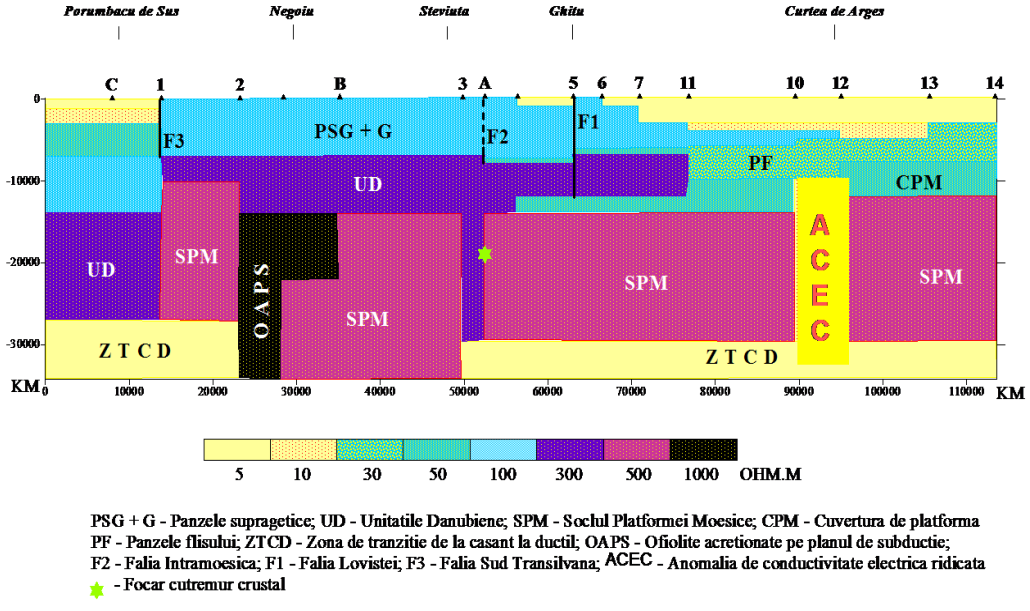

PSG + G - Panzele supragetice; UD - Unitatile Danubiene; SPM - Soclul Platformei Moesice; CPM - Cuvertura de platforma
PF - Panzele flisului; ZTCD - Zona de tranzitie de la casant la ductil; OAPS - Ofiolite acretionate pe planul de subductie;
F2 - Falia Intramoesica; F1 - Falia Lovistei; F3 - Falia Sud Transilvana; ACEC - Anomalia de conductivitate electrica ridicata
- Focar cutremur crustal

Fig. 3.2.5. 2-D Model for the resistivity along profile III-III'

References

Mutihac, V., Structura geologică a teritoriului României, Ed. Tehnică, București, 1990.

Paucă, M., Etapele genetice ale Depresiunii Transilvaniei, S.C.G.G.G., Geol., XVII, 2. 1972.

Pinna, E., Soare, A., Stanica, D., Stanica, M., Carpathian conductivity anomaly and its relation to deep structure of the substratum, Acta Geod. Geoph. Mont. Hung. 27(1), pp 35–45, 1992.

Stanica, M., Stanica, D**.,** Marin-Furnica, C., The Placement of the Trans-European Suture Zone by Electromagnetic Arguments on the Romanian Territory. Earth, Planets and Space, 51, 1073-1078, 1999.

Chapter IV. Toward a model for the distribution of the surface geoelectric field produced by hazardeous geomagnetic variations. Case study – the Romanian territory

The strong variations of the magnitude and direction of the geomagnetic field during geomagnetic storms and substorms triggered by the interaction with the magnetosphere and ionosphere of coronal mass ejections (CMEs), mainly during the maximum solar activity, and by the high speed streams (HSSs) in the solar wind, especially in the declining phase of the 11-year solar cycle, induce in the Earth and in the power grid systems certain variable electric fields that produce, in turn, electric currents known as **geophysically induced currents (GICs)**. This current type has been studied since the middle of the 19th century, following observations from communication cables. In the years following the catastrophic breakdown of the power network in Quebec, Canada, during the severe magnetic storm of March 13/14, 1989, a special interest has been given to induced currents both in Canada and in the northern countries (Blais and Metsa, 1994; Boteler and Pirjola, 1998; Viljanen, 1997; Pirjola and Viljanen, 1998; Beamish et al., 2002), as being most affected by such a phenomenon because of the proximity of the auroral current system. On the other hand, it has been shown that the effects of induction could be significant at more southern latitudes (British Isles, South Africa) (Beamish et al., 2002). At present the European project EURISGIC is running, that will produce as a prototype the first forecasting service for GICs in power networks. Principles have been presented, e. g., by Viljanen et al. (2012).

The computation of GIC in a given system of conductors is done in two steps: (1) the determination of the electric field associated to geomagnetic variations, step that does not depend on the concrete technological system, and (2) the determination of GIC in the given technological system. In the present research contract we aimed at tackling the first aspect, and in the present stage we aimed at approaching, in a first instance, of a study based on recordings provided by the Surlari geomagnetic observatory, the only observatory in the Romanian area. In the next phase (2015) we shall approach also the determination of some quantitative elements regarding the GIC hazard in the national power network.

4.1. The computing model

Generaly, the horizontal electric field (Ex, Ey) produced by the variable magnetic field is related to the magnetic field (Bx, By) through the impedance $Z(\omega)$ of the plane wave by means of which the propagation of the geomagnetic disturbance is approximated:

$$E_x(\omega) = \frac{Z(\omega)}{\mu_0} B_y(\omega), E_y(\omega) = \frac{Z(\omega)}{\mu_0} B_x(\omega) \quad (1)$$

In this relation, ω is the angular frequency of the plane wave, x and y refer to the North and, respectively East directions, and μ_o is the vacuum permeability.

In case of an Earth viewed as a halfspace with the conductivity σ, and the propagation of the geomagnetic disturbance in the inside as that of a vertical plane wave, the surface electric field is described by the relationship (Viljanen and Pirjola, 1989):

$$E_y(t) = -\frac{1}{\sqrt{\pi\mu_0\sigma}} \int_{-\infty}^{t} \frac{g_x(u)}{\sqrt{t-u}} du \quad (2)$$

in which g_x means the time derivative of the field B.

The integral in eq. (2) is replaced in practice by a sum, and the lower integration limit by M = 720. That is, in the summation the variations produced in a 12 hours interval before the first time moment T_N, in which the electric field is calculated, are taken into account too. The geomagnetic recording should appear as minute values, the standard of the INTERMAGNET network:

$$E(T_N) = \frac{2}{\sqrt{\pi\mu_0\sigma}} (R_{N-1} - R_N - \sqrt{M} b_{N-M}) \quad (3)$$

$$R_N = \sum_{n=N-M+1}^{N} b_n \sqrt{N-n+1} \quad (4)$$

To solve the problem, a computer code, presented in the next section, was worked out. By means of this program, calculations for several geomagnetic storms in the solar cycle 23 were done. The results for the Surlari observatory were compared to results for the Nurmijarvi observatory (Finland), located in the auroral zone, in which the effects of the geomagnetic variations are stronger.

4.2. Results

4.2.1. The computer code worked out in the present stage of the contract

Based on eqs. (2), (3), and (4) a MATLAB computer code, presented in the following, was worked out.

```
load data.dat
%input parameters
Bx=data(:,2);            % North geomagnetic element
By=data(:,3);            % East geomagentic component
time=data(:,1);          %time interval in minutes
mu0=4*pi*10^(-7);        %vacuum permeability
sigma;                   %electrical conductivity
N=length(SUA);
M                        %time in minutes before the event

%time derivative
dBx=diff(Bx);
dBy=diff(By);
dt=diff(time);
gtx=dBx./dt;
gty=dBx./dt;

i=(N-M+1):N;
Ci=sqrt(i);
Citr=transpose(Ci);
bxi=(Bx(i)-Bx(i-1))./60;
byi=(By(i)-By(i-1))./60;
Rx=bxi.*Citr;
Ry=byi.*Citr;
RNx=sum(Rx);
RNy=sum(Ry);
bxibef=(Bx(i-1)-Bx(i-2))./60;
byibef=(By(i-1)-By(i-2))./60;

Cibefore=sqrt(i+1);
Cibef=transpose(Cibefore);
Rxbef=bxibef.*Cibef;
Rybef=byibef.*Cibef;
RNxbef=sum(Rxbef);
RNybef=sum(Rybef);
Ey=((2/sqrt(pi*mu0*sigma))*((RNxbef- RNx) -(sqrt(M))*bxi(i-M)))*10^(-3);
Ex=((2/sqrt(pi*mu0*sigma))*((RNybef- RNy) -(sqrt(M))*byi(i-M)))*10^(-3);

figure(1)
subplot(3,1,1), plot(Bx), title('Bx')
subplot(3,1,2), plot(gtx), title('dBx/dt')
subplot(3,1,3), plot(Ey), title('Ey')

figure(2)
subplot(3,1,1), plot(By), title('By')
subplot(3,1,2), plot(gty), title('dBy/dt')
subplot(3,1,3), plot(Ex), title('Ex')
```

4.2.2. The variation of the geoelectric field

To illustrate the way the code works, we chose the time interval that contains the geomagnetic storm of November 8, 2004, that had a Dst minimum of -374 nT (Fig. 4.2.1).

To exemplify, we used data from two geomagnetic observatories, namely the national

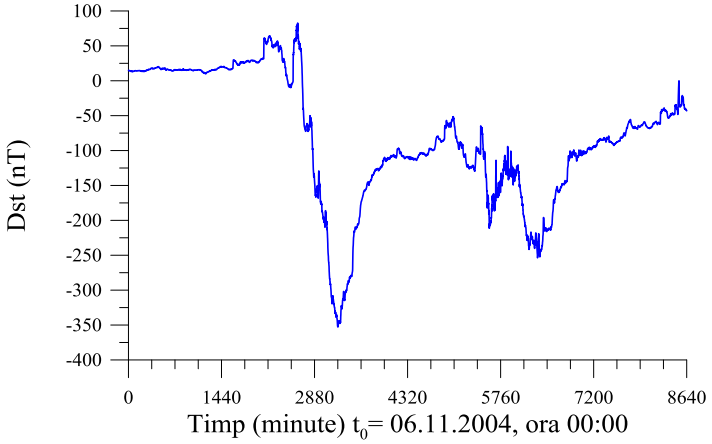

Fig. 4.2.1. The variation of the Dst index for the geomagnetic storm of November 7, 2004

geomagnetic observatory, Surlari (SUA), located at midlatitude, and the Finish one, Nurmijarvi (NUR), located under the auroral current system. The geoelectric field was calculated for both horizontal components, Ex and Ey, based on geomagnetic recordings Bx and By, using specific electric conductivity for the two locations, of 0.10 $\Omega^{-1}m^{-1}$ for SUA and of $1x10^{-4}$ $\Omega^{-1}m^{-1}$ for NUR. The results are presented in Figs. 4.2.2 and 4.2.3.

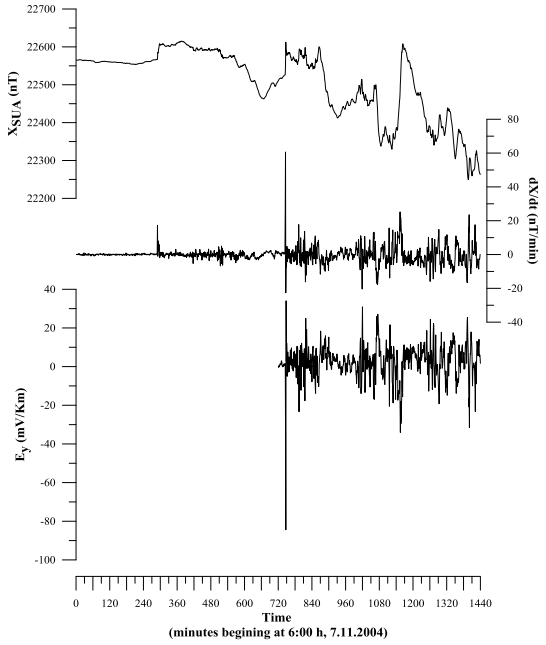

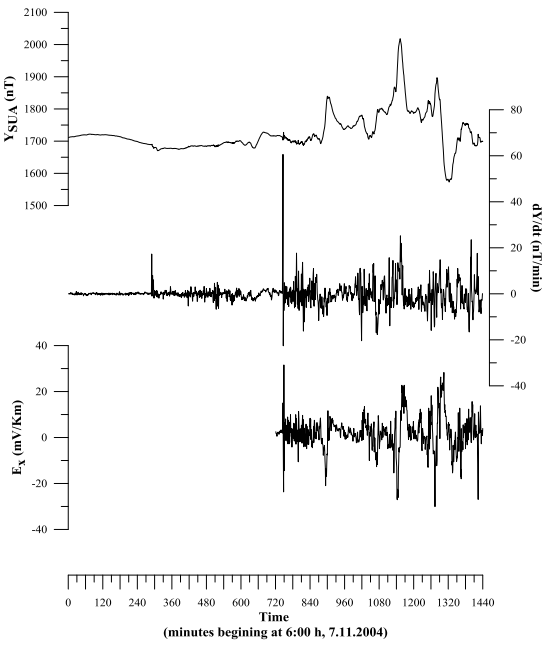

Fig. 4.2.2. The surface geoelectric field for SUA (lower plots). In the same figure the variation of the components X and Y (upper plots) and their time derivative (middle plots) are also given

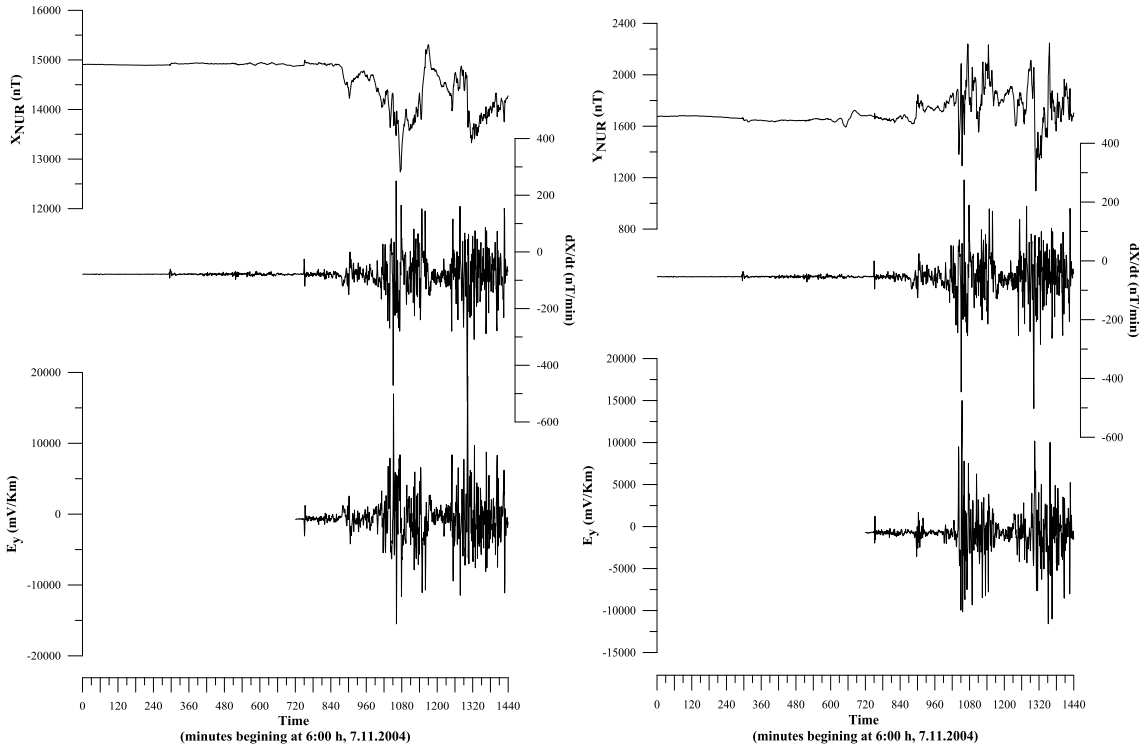

Fig. 4.2.3. The surface geoelectric field for NUR observatory (lower plots). In the same figure the variation of the components X and Y (upper plots) and their time derivative (middle plots) are also given

A comparative view of the results for the two observatories shows, even at this stage of research, the following:

- The more pronounced geoelectric component is directed East-West;
- The amplitude difference is of the order of tens of mV/km in case of SUA, and of thousands of mV/km in case of NUR;
- The sudden storm commencement (SSC, h=10:57 TU, November 7, 2004) is more pronounced at SUA latitude than at the NUR latitude and produces a significant variation of the electric field at SUA when compared with later variations. The amplitude differences reverse in case of NUR, where the effects of auroral current dominate.

References

Beamish D., Clark TDG., Clarke E., 2002. Thompson AWP.

Blais G., Metsa P., 1994. Solar-Terrestrial Predictions IV, 108-130.

Boteler, D. H. and Pirjola, R. J., The complex-image method for calculating the magnetic and electric fields produced at the surface of the Earth by the auroral electrojet, Geophys. J. Int., 132,31–40, 1998.

Pirjola, R. and Viljanen, A., Complex image method for calculating electric and magnetic fields produced by an auroral electrojet of a finite length, Ann. Geophysicae, 16, 1434–1444, 1998.

Viljanen, A. and Pirjola, R., Statistics on geomagnetically-induced currents in the Finnish 400 kV power system based on recordings of geomagnetic variations. J.Geomagnetism and Geoelectricity, 41, 411–420, 1989.

Viljanen, A., The relation between geomagnetic variations and their time derivatives and implications for estimation of induction risks, Geophys. Res. Lett., 24, 631-634, 1997.

Viljanen, A., Pirjola, R., Wik, M., Adam, A., Pracser, E., Sakharov, Y. and Katkalov, J., Continental scale modelling of geomagnetically induced currents, J. Space Weather Space Clim. 2, A17, doi: 10.1051/swsc/2012017, 2012.

Chapter IV. Dissemination of results

In the report period 3 papers have been submitted for pubication, namely:

- Beşliu-Ionescu, D., Mariş Muntean, G., Lăcătuş, D.A., Paraschiv, A.R., Mierla, M., Detailed Analysis of a Geoeffective ICME Triggered by the March 15, 2013 CME, Romanian Geophysical Journal, 2014, accepted.
- Stefan, C., Application of the Radon transform to the study of traveling speeds of core geomagnetic field features. Case study – The ~80-year variation, Romanian Geophysical Journal, 2014, accepted.
- Dobrica, V., Demetrescu, C., Mandea, M., Geomagnetic field declination: from decadal to centennial scales, Journal of Geophysical Research B, 2014, submitted.

Also, during 2014, the team members of the research contract participated at 5 international scientific meetings, with 12 presentations:

- Demetrescu C., Stefan C., Dobrica V., External field noise in main field models at Earth's surface and at core/mantle boundary, *European Geosciences Union General Assembly, Vienna, Austria, 27 April – 02 May 2014*
- Demetrescu C., Stefan C., Dobrica V., Space climate. On geoeffective solar activity during Maunder and Dalton grand minima, *European Geosciences Union General Assembly, Vienna, Austria, 27 April – 02 May 2014*
- Stefan C., Demetrescu C., Dobrica V., On the characteristics of a residual external signal seen in coefficients of main geomagnetic field models, *European Geosciences Union General Assembly, Vienna, Austria, 27 April – 02 May 2014*
- Greculeasa, R., Dobrica, V., Demetrescu, C., The disturbed geomagnetic field at European observatories. Sources and significance, *European Geosciences Union General Assembly, Vienna, Austria, 27 April – 02 May 2014*
- Maris Muntean, G., Besliu-Ionescu, D., Dobrica, V., Lacatus, D.A., Paraschiv, A.R., Fast Solar Wind and Geomagnetic Variability during the 24th Solar Cycle (2009 - 2013), *European Geosciences Union General Assembly, Vienna, Austria, 27 April – 02 May 2014*
- Besliu-Ionescu, D., Lacatus, D.A., Paraschiv, A.R., Mierla, M., Geoeffective CMEs Associated with Seismically Active Flares, *European Geosciences Union General Assembly, Vienna, Austria, 27 April – 02 May 2014*
- Stefan C., Demetrescu C., Dobrica V., A Tentative Reconstruction of the Dst Index back to 1840, Based on Long Time-Span Models of the Core Magnetic

Field, *The Sixth Workshop "Solar influences on the magnetosphere, ionosphere and atmosphere", Sunny Beach, Bulgaria, 26-30 May 2014*

- Maris Muntean, G., Besliu-Ionescu, D., Georgieva, K., Kirov, B., Analysis of the Geomagnetic Activity during the SC 24 Maximum Phase, *The Sixth Workshop "Solar influences on the magnetosphere, ionosphere and atmosphere", Sunny Beach, Bulgaria, 26-30 May 2014*
- Demetrescu C., Stefan C., Dobrica V., 400 years of space climate information from long-term main geomagnetic field models, *11th Annual Asia Oceania Geosciences Society (AOGS) Assembly, Sapporo, Japan, 28 July – 01 August 2014*
- Mariș Muntean, G., Beșliu-Ionescu, D., Dobrică, V., Lăcătuș, D.A., Paraschiv, A.R., Sources and Complexity of the Strong Geomagnetic Storms during the Maximum Phase of Solar Cycle 24, *11th Annual Asia Oceania Geosciences Society (AOGS) Assembly, Sapporo, Japan, 28 July – 01 August 2014*
- Mariș Muntean, G., Besliu-Ionescu, D., Mierla, M., Detailed analysis of two intense geomagnetic storms during solar cycle 24, *40th COSPAR Scientific Assembly, Moscova, Rusia, 2-10 August 2014*
- Maris Muntean, G., Besliu-Ionescu, D., Mierla, M., March 2013 ICMEs and their Geomagnetic Effects, *11th European Space Weather Week, Liege, Belgium, November 17-21, 2014*

To close this report, we mention that the web page of the project, http://www.geodin.ro/IDEI2011/engl/index.html, was updated.